Cryogenic Deuterium and Deuterium–Tritium Direct-Drive Implosions on OMEGA

Introduction

To ignite the deuterium–tritium (DT) fuel in a conventional, hot-spot ignition scheme in inertial confinement fusion (ICF), ion temperature and areal density of the central, lower-density region (hot spot) of the final fuel assembly must be sufficient to create fuel self-heating by alpha particles produced as a result of fusing D and T (Refs. 1 and 2). In addition, the areal density (ρR) of the main fuel must be large enough to provide confinement time sufficient to burn a significant portion of that fuel. A typical target consists of a higher-density shell filled with a lower-density fuel vapor. The shell has an outer layer of ablator material and an inner layer of frozen fuel. To compress the main fuel layer and initiate a burn wave propagating from the vapor through the main fuel, the shell is accelerated inward by a temporally shaped pressure drive created by laser energy that is delivered either directly to the target (direct drive) or indirectly by converting its energy to x rays inside the hohlraum (indirect drive).[1,2] As convergence causes pressure to build up in the vapor, the shell begins to decelerate when the vapor pressure exceeds shell pressure and an outgoing shock wave is launched into the incoming shell. During deceleration, hot-spot areal density and temperature increase as the shell's kinetic energy is converted into internal energy of the hot spot and main fuel. Achieving ignition conditions requires the areal density of the hot spot to exceed the stopping range of the alpha particles produced by fusing D and T. This leads to $(\rho R)_{hs} \geq 0.3$ g/cm^2 (Refs. 1 and 2). In addition, the hot-spot ion temperature T_{hs} must be larger than ~5 keV so that the alpha heating exceeds bremsstrahlung losses.[1,2] Since both hot-spot areal density and temperature depend on in-flight shell kinetic energy, there is a threshold value of this energy below which a target fails to ignite.

A target design starts by calculating how much energy the drive pressure must provide to the shell so ignition requirements are met at stagnation. Numerical simulations give the following expression for the minimum shell kinetic energy required for ignition:[3,4]

$$E_{k,\min}(\text{kJ}) = 51\,\alpha^{1.9} \left(\frac{V_{imp}}{3 \times 10^7} \right)^{-5.9} \left(\frac{p_a}{100\ \text{Mbar}} \right)^{-0.8}. \quad (1)$$

This expression depends on the following in-flight hydrodynamic parameters, crucial for achieving ignition: (1) the peak in mass-averaged main fuel velocity (implosion velocity) V_{imp}; (2) the in-flight fuel adiabat α [defined as the ratio of the shell pressure p to the Fermi-degenerate pressure at shell density ρ; for DT fuel, $p \simeq \mu\alpha\rho^{5/3}$ and $\mu = 2.2$ Mbar$/$(g/cm$^{3/5}$)]; and (3) the drive (ablation) pressure p_a. Even though Eq. (1) provides a very useful scaling law, it gives very little insight into the physical processes that determine this scaling. To provide such an insight, a simplified model of hot-spot formation is developed and presented next.

1. A Simple Ignition Model

To calculate minimum shell kinetic energy of an igniting target, nearly all this energy is assumed to be converted into the internal hot-spot and fuel energy at stagnation,

$$E_k \sim p_{\max} R^3 \sim \left(\rho_{hs} T_{hs} R \right)^3 / p_{\max}^2, \quad (2)$$

where $p_{\max} \sim \rho_{hs} T_{hs} / m_i$ is the peak hot-spot pressure and m_i is ion mass. Since the minimum value of product $(\rho R)_{hs} T_{hs}$ is 0.3 g/cm$^2 \times 5$ keV, as described earlier, then[2]

$$E_{k,\min} \sim 1 / p_{\max}^2 \quad (3)$$

and calculation of $E_{k,\min}$ is reduced to determine the peak hot-spot pressure.

The maximum pressure is calculated by assuming that the hot-spot radius at peak convergence is R, and a fraction f_{shl} of shell kinetic energy $E_k = MV_{imp}^2 / 2$ has been transferred at that time to the hot-spot internal energy $2\pi p_{\max} R^3$, where M is the unablated shell mass. Then, the maximum hot-spot pressure is

$$p_{\max} \sim f_{shl} E_k / R^3. \quad (4)$$

With the goal of expressing $E_{k,\min}$ and $p_{\max}$ in terms of in-flight shell parameters, stagnation variables must be related to these at the beginning of shell deceleration. Since the hot spot is adiabatic during deceleration,[4,5] $p_{\max}$ can be written in

terms of vapor pressure p_d and radius of vapor region R_d at the beginning of shell deceleration:

$$p_{max} = p_d (R_d / R)^5. \tag{5}$$

Equating the right-hand sides of Eqs. (4) and (5) gives a hot-spot convergence ratio during deceleration,

$$\frac{R_d}{R} \sim \sqrt{\frac{f_{shl} E_k}{p_d R_d^3}}. \tag{6}$$

Then, using Eqs. (5) and (6) defines the maximum hot-spot pressure as a ratio of the shell's kinetic energy to the internal energy of the vapor at the beginning of deceleration:[5]

$$p_{max} \sim p_d \left(\frac{f_{shl} E_k}{p_d R_d^3} \right)^{5/3} \sim p_d \left(\frac{f_{shl} M}{p_d R_d^3} \right)^{5/2} V_{imp}^5. \tag{7}$$

For $f_{shl} = 1$, Eqs. (3) and (7) give $p_{max} \sim V_{imp}^5$ and $E_{k,min} \sim V_{imp}^{-10}$, similar to the result of the isobaric model.[6] The fraction f_{shl}, however, is smaller than unity and depends on in-flight shell parameters. Keeping in mind that the shell is decelerated by the outgoing shock wave, f_{shl} can be defined as a fraction of the shell mass (an effective mass M_{eff}) overtaken by this shock while the hot spot converges inward. In the strong shock limit, the Hugoniot conditions across the shock give

$$M_{eff} \equiv f_{shl} M \sim \sqrt{\rho_{shl} p_{max}} R^2 \Delta t, \tag{8}$$

where ρ_{shl} is the shell density ahead of the shock front. The hot-spot time of confinement by the shell inertia is determined by Newton's law, $M_{eff} R / (\Delta t)^2 \sim p_{max} R^2$, which yields[7]

$$\Delta t \sim \sqrt{M_{eff} / p_{max} R}. \tag{9}$$

Then, Eqs. (8) and (9) lead to

$$M_{eff} \sim \rho_{shl} R^3. \tag{10}$$

With the help of the latter equation, Eq. (4) yields intuitively simple scaling

$$p_{max} \sim \rho_{shl} V_{imp}^2. \tag{11}$$

The maximum pressure, however, does not scale as V_{imp}^2, as Eq. (11) would suggest, since ρ_{shl} is different from the in-flight shell density. As the unshocked part of the incoming shell

keeps converging during deceleration, its density ρ_{shl} increases inversely proportional to the surface area:

$$\rho_{shl} \simeq \rho_d \left(\frac{R_d}{R} \right)^2. \tag{12}$$

Combining Eqs. (5), (11), and (12) defines the hot-spot convergence ratio in terms of in-flight shell quantities

$$\frac{R_d}{R} \sim \left(\frac{V_{imp}^2 \rho_d}{p_d} \right)^{1/3}. \tag{13}$$

Substituting Eq. (13) into Eqs. (10) and (12) gives the effective shell mass and ρ_{shl}:

$$M_{eff} \sim \rho_d R_d^3 \frac{R_d}{R} \sim \rho_d R_d^3 \left(\frac{p_d}{\rho_d V_{imp}^2} \right)^{1/3} \tag{14}$$

and

$$\rho_{shl} \sim \rho_d \left(\frac{V_{imp}^2 \rho_d}{p_d} \right)^{2/3}. \tag{15}$$

Finally, the scaling for the maximum pressure is obtained by combining Eqs. (7) and (14):

$$p_{max} \sim \rho_d V_{imp}^2 \left(\frac{V_{imp}^2 \rho_d}{p_d} \right)^{2/3} = p_d \left(\frac{V_{imp}^2 \rho_d}{p_d} \right)^{5/3}. \tag{16}$$

Pressure at the beginning of the deceleration phase is proportional to the drive ablation pressure, $p_d \sim p_a$, and shell density is related to the drive pressure through the in-flight shell adiabat α, $p_d (\text{Mbar}) \sim 2.2 \, \alpha \rho_d^{5/3}$. This gives

$$p_{max} \sim \frac{p_a^{1/3} V_{imp}^{10/3}}{\alpha}. \tag{17}$$

This scaling of p_{max} with V_{imp} is similar to that derived using self-similar analysis,[8] which leads to $p_{max}^{\text{self-similar}} \sim V_{imp}^3$. Substituting Eq. (17) back into Eq. (3) gives a scaling law similar to that obtained using simulation results [see Eq. (1)]:

$$E_{k,min} \sim 1 / p_{max}^2 \sim V_{imp}^{-20/3} p_a^{-2/3} \alpha^2. \tag{18}$$

Equation (17) shows that the maximum pressure has a weaker implosion velocity dependence than $V_{\rm imp}^5$ obtained assuming that all kinetic energy of the shell is transferred to the internal energy of the fuel at stagnation. The weaker dependence is due to the fact that the kinetic energy fraction contributing to the fuel's internal energy is proportional to the fraction of the shell mass overtaken by the outgoing shock wave during the hot-spot confinement time. Several competing effects define this fraction: First, the mass flux per unit area across the shock increases with hot-spot convergence since both shell density $\rho_{\rm shl}$ and maximum pressure $p_{\rm max}$ increase with R_d/R [see Eqs. (5) and (12)], so $\sqrt{\rho_{\rm shl} p_{\rm max}} \sim \sqrt{\rho_d p_d} \left(R_d/R\right)^{7/2}$. Multiplied by the surface area of the shock front, the mass flux across the shock is $\sqrt{\rho_{\rm shl} p_{\rm max}}\, R^2 \sim \sqrt{\rho_d p_d}\, R_d^2 \left(R_d/R\right)^{3/2}$. The convergence ratio increases with the implosion velocity, as shown in Eq. (13), giving

$$\text{mass flux} \sim \sqrt{\rho_{\rm shl} p_{\rm max}}\, R^2 \sim V_{\rm imp}. \tag{19}$$

The confinement time, on the other hand, decreases with convergence ratio and implosion velocity. Indeed, writing $\Delta t \sim R/V_{\rm imp}$ [this can be obtained by substituting Eqs. (10) and (11) into Eq. (9)] and using Eq. (13) gives

$$\text{confinement time} \sim \frac{R}{V_{\rm imp}} \sim \left(\frac{R_d}{R}\right)^{-5/2} \sim V_{\rm imp}^{-5/3}. \tag{20}$$

Then, the product of mass flux and confinement time gives the effective mass and fraction of kinetic energy that contributes to the stagnation pressure $M_{\rm eff} \sim f_{\rm shl} \sim V_{\rm imp}^{-2/3}$, in agreement with Eq. (14). Negative power in velocity dependence of the effective mass changes pressure scaling from $V_{\rm imp}^5$ to $V_{\rm imp}^{10/3}$.

The maximum pressure, on the other hand, has a stronger dependence on $V_{\rm imp}$ than that given by the dynamic pressure argument $p_{\rm max} \sim \rho_{\rm shl} V_{\rm imp}^{10/2}$. This is due to convergence effects and an increase in the unshocked shell density during deceleration. Since $\rho_{\rm shl}$ rises with convergence ratio, as shown in Eq. (12), the maximum pressure scales as

$$p_{\rm max} \sim \left(\rho_{\rm in\ flight} V_{\rm imp}^{2\times 2/3}\right) V_{\rm imp}^2 \sim V_{\rm imp}^{10/3},$$

in agreement with Eq. (17).

Since $E_{\rm k,min}$ is strongly dependent on the implosion velocity, as shown in Eqs. (1) and (18), it is crucial that a shell reaches

the designed value of $V_{\rm imp}$ to achieve ignition in an experiment. The minimum $V_{\rm imp}$ can be estimated by the following argument: Balancing a fraction of the kinetic energy of the shell and the internal energy of the fuel yields

$$MV_{\rm imp}^2 \Big/ 2 > 2\pi p_{\rm max} R^3. \tag{21}$$

For fully ionized gas with ion charge Z and ion mass $m_{\rm i}$,

$$p_{\rm max} = (1+Z)\rho_{\rm hs} T_{\rm hs}\big/ m_{\rm i}.$$

For DT fuel this gives $p_{\rm max} \simeq 4\rho_{\rm hs} T_{\rm hs}/m_{\rm p}$, where $m_{\rm p}$ is proton mass. Finally, writing shell mass at stagnation as $M \sim 4\pi R^2 \rho_{\rm fuel}\Delta$ leads to

$$V_{\rm imp} > \sqrt{\frac{4}{5}\frac{(\rho R)_{\rm hs}}{(\rho\Delta)_{\rm fuel}}\frac{T_{\rm hs}}{m_{\rm p}}}, \tag{22}$$

where $\rho_{\rm fuel}$ and Δ are the density and thickness of compressed fuel, respectively. To create a hot spot and trigger burn propagation into the cold fuel, the hot-spot areal density and temperature must exceed, as discussed earlier, $(\rho R)_{\rm hs} T_{\rm hs} > 0.3\ {\rm g/cm}^2 \times 5\ {\rm keV}$. To burn enough cold fuel and achieve gain = fusion energy/laser energy > 1 requires, on the other hand, $(\rho\Delta)$fuel $> 1\ {\rm g/cm}^2$ (Refs. 1 and 2). Substituting these three conditions back into Eq. (22) gives

$$V_{\rm imp} > 3 \times 10^7\ {\rm cm/s}. \tag{23}$$

This leads to a requirement on stagnation pressure $p_{\rm max}$. Indeed, the ablation pressure in an ICF implosion is $p_{\rm a} \sim 100\ {\rm Mbar}$, and the effective dynamic pressure of the accelerated shell at $V_{\rm imp} = 3 \times 10^7\ {\rm cm/s}$ and $\alpha = 1$ is $\rho V^2 \simeq (100/2.2)^{3/5}$ $[3 \times 10^7]^2 \simeq 9\ {\rm Gbar}$. In general, $\rho \simeq \left[p({\rm Mbar})/2.2\,\alpha\right]^{3/5}$ and the dynamic pressure is

$$\text{dynamic pressure}_{\rm in\ flight} \simeq$$

$$9\left(\frac{p_{\rm a}}{100\ {\rm Mbar}}\right)^{3/5}\alpha^{-3/5}\left(\frac{V_{\rm imp}}{3\times 10^7}\right)^2\ {\rm Gbar}. \tag{24}$$

An additional amplification in dynamic pressure is due to shell convergence during deceleration. As described earlier, unshocked-shell density amplification is proportional to the hot-spot convergence ratio to the second power [see Eq. (12)]. According to Eq. (13), the hot spot converges by a factor of 4.4 during deceleration for $\alpha \sim 1$ and $V_{\rm imp} \sim 3 \times 10^7$ cm/s. This

gives an additional increase by a factor of $4.4^2 = 20$ in the dynamic pressure, leading to a maximum hot-spot pressure in an igniting target of $p_{max} > 200$ Gbar, or for a given implosion velocity and drive pressure,

$$p_{max} \simeq 180 \left(\frac{p_a}{100 \text{ Mbar}} \right)^{1/3} \alpha^{-1} \left(\frac{V_{imp}}{3 \times 10^7} \right)^{10/3} \text{ Gbar.} \quad (25)$$

Using the numerical factor obtained in Eq. (25), one can recover a numerical factor in Eq. (18) as well:

$$E_{k,min} \simeq 30 \, \alpha^2 \left(\frac{V_{imp}}{3 \times 10^7} \right)^{-20/3} \left(\frac{p_a}{100 \text{ Mbar}} \right)^{-2/3} \text{ kJ.} \quad (26)$$

The numerical coefficient in Eq. (26) is 40% smaller than that in the fitting formula shown in Eq. (1). This is a consequence of the fact that only a fraction f_{shl} of the total shell kinetic energy is transferred to the fuel at stagnation. Typically, $f_{shl} \sim 0.5$ to 0.6, which brings the numerical coefficient in Eq. (26) in closer agreement with the numerical result.

2. Sensitivity of Ignition Condition on Implosion Parameters

The minimum shell kinetic energy required for ignition depends strongly on the shell's velocity and adiabat [see Eq. (1)]. When a particular target design is considered for an ignition experiment, one of the important design parameters is margin [this is also referred to as an ignition threshold factor (ITF)][9] defined as the ratio of the shell kinetic energy E_k to its minimum value required for ignition $E_{k,min}$,

$$\text{ITF} = \frac{E_k}{E_{k,min}} \,. \quad (27)$$

In using Eq. (1) to determine $E_{k,min}$, one must keep in mind that Eq. (1) does not account for asymmetry effects (such as shell and hot-spot nonuniformity growth, mix of ablator material and fuel, etc.). A more-complete analysis using 2-D and 3-D hydrodynamic simulations results in correction factors related to these effects (for details, see Ref. 9). Since the main purpose of this article is to address accuracy in the modeling of average 1-D hydrodynamic parameters, the terms proportional to multidimensional effects will be neglected.

Robustness of a particular design is determined by how much uncertainty in velocity, adiabat, and the drive pressure it can tolerate before the probability of achieving ignition becomes very small. Such maximum uncertainty values depend on ITF.

The target fails to ignite if the shell's kinetic energy E_k in an experiment is lower than the ignition energy threshold $E_{k,min}$ or the actual energy threshold $E_{k,min}$ is higher than calculated $E_{k,min}$ as a result of inaccuracies in modeling of hydro-dynamic quantities. If E_k^{design} and $E_{k,min}^{design}$ are design values of the shell's kinetic energy and energy threshold, respectively, and ITF $= E_k^{design} / E_{k,min}^{design}$, then the maximum deviations in V_{imp}, α, and p_a (denoted as δV_{imp}, $\delta \alpha$, and δp_a, respectively) from predictions are determined from the condition $E_k^{limit} / E_{k,min}^{limit} = 1$, where $E_k^{limit} = M(V_{imp} - \delta V_{imp})^2 / 2$,

$$E_{k,min}^{limit} = E_{k,min}(\alpha + \delta \alpha, V_{imp} - \delta V_{imp}, p_a - \delta p_a),$$

$E_k^{design} = M V_{imp}^2 / 2$, and $E_{k,min}^{design} = E_{k,min}(\alpha, V_{imp}, p_a)$.

This reads as

$$1 = \text{ITF} \left(1 - \frac{\delta V_{imp}}{V_{imp}} \right)^{7.9} \left(1 + \frac{\delta \alpha}{\alpha} \right)^{-1.9} \left(1 - \frac{\delta p_a}{p_a} \right)^{0.8}. \quad (28)$$

Since it is very difficult to assess the fuel adiabat by a direct measurement, the adiabat increase $\delta \alpha$ is replaced in this analysis with energy deposited in the fuel ΔE that leads to an adiabat increase $\delta \alpha$. This energy is expressed in terms of a fraction ε_E of the shell kinetic energy $\Delta E = \varepsilon_E E_{k,0}$. To relate $\delta \alpha$ and ΔE, we write internal energy as a product of pressure and volume $E = 3/2 \, pV$. Replacing pressure by the drive ablation pressure p_a and the fuel volume by fuel mass over shell density, $V = M/\rho$, gives $E = 3p_a M/2\rho$. Shell density is related to the ablation pressure as $\rho \sim (p_a/\alpha)^{3/5}$. Then, collecting all appropriate numerical coefficients leads to

$$E(\text{kJ}) = 1.5 \left(\frac{p_a}{100 \text{ Mbar}} \right)^{2/5} \alpha^{3/5} M(\text{mg}). \quad (29)$$

Fixing shell mass and drive pressure gives $1 + \delta \alpha/\alpha = (1 + \Delta E/E_0)^{5/3}$. Then, Eq. (28) takes the form

$$\left(1 - \frac{\delta V_{imp}}{V_{imp}} \right)^{-7.9} \left[1 + \frac{30 \, \varepsilon_E \left(V_{imp} / 3 \times 10^7 \right)^2}{\left(p_a / 100 \text{ Mbar} \right)^{2/5} \alpha^{3/5}} \right]^{3.1}$$

$$\times \left(1 - \frac{\delta p_a}{p_a} \right)^{-0.8} = \text{ITF.} \quad (30)$$

Figure 130.16 plots (a) the reduction in shell velocity, (b) shell preheat as a percentage fraction of the shell's kinetic energy, and (c) reduction in drive pressure that lead to ignition failure in a design with a given value of ITF. Figure 130.16 shows that for NIF-scale ignition designs with ITF ~ 3.5 to 5, ignition fails if velocity reduction is greater than ~15% and the shell is preheated by more than ~1% of the shell's kinetic energy. The drive pressure, according to Fig. 130.16(c), can be reduced as much as 80% before ignition will fail. This number, however, does not account for a reduction in the implosion velocity associated with reduced drive. Therefore, Fig. 130.16(c) must be used in combination with Fig. 130.16(a). In addition to ignition failure caused by a significant deviation from predicted 1-D hydrodynamic parameters (velocity, adiabat, drive pressure), other failure mechanisms are due to asymmetries in an implosion. Nonuniformity sources caused by both target imperfections (such as ice roughness and ablator roughness) and asymmetry in laser illumination are amplified by the Rayleigh–Taylor (RT) and Richtmyer–Meshkov (RM) instabilities[1,2] during an implosion. Nonuniformity growth could either disrupt the shell or lead to significant hot-spot distortions. The distortion region width inside the hot spot exceeding 20% to 40% of the 1-D hot-spot radius is typically sufficient to reduce alpha-particle production and ion temperature and quench the burn.[7]

Even though control of the multidimensional effect is one of the main challenges for any ignition design, validation of code ability to adequately model target-drive efficiency and the amount of the fuel preheat is a primary goal of the ICF experiments. This article will describe how these global hydrodynamic parameters predicted by hydrosimulations were experimentally validated using direct-drive implosions on OMEGA.

Early Direct-Drive Target Designs and Target Stability Properties

1. All-DT, Direct-Drive, NIF-Scale Ignition Target Design

The original direct-drive target design[10,11] for the National Ignition Facility (NIF) Laser System[12] is a 350-μm-thick, solid-DT layer inside a very thin (~3-μm) plastic shell (shown in Fig. 130.17). Because the plastic shell ablates early in the pulse and the DT layer acts as both the main fuel and ablator, this design is referred to as an "all-DT" design. The fact that the ablator and the main fuel are the same material (DT) has several advantages: (1) It eliminates the interface between the fuel and ablator. Any mismatch in density or opacity between two neighboring materials in the shell usually leads to an enhancement in the early-time perturbation growth or the RT instability growth factor.[13] (2) Because of its initial low density, DT gives both the lowest in-flight aspect ratio (IFAR)
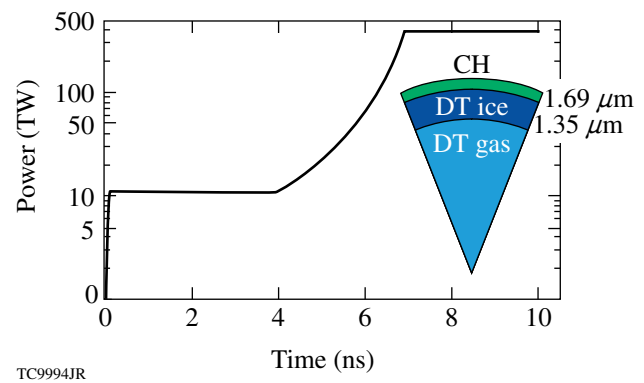

TC9994JR

Figure 130.17
An $\alpha = 3$, "all-DT," 1.5-MJ, direct-drive–ignition target design with a 1-D gain of 45.
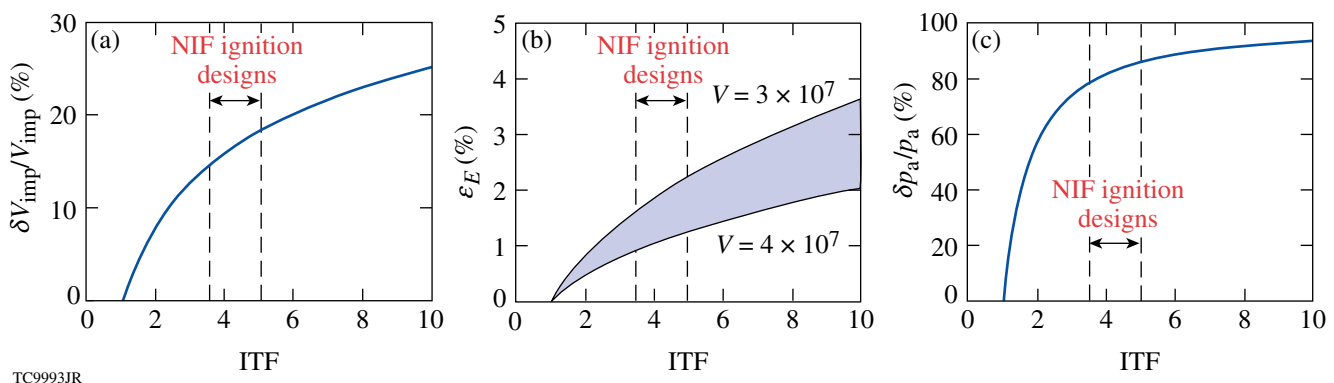

TC9993JR

Figure 130.16
(a) Maximum velocity reduction, (b) maximum preheat energy as fractions of the shell's kinetic energy, and (c) maximum pressure reduction versus ITF.

for the same shell mass and the largest ablative stabilization factor in the RT instability growth rate formula compared to other ablator materials [see **Rayleigh–Taylor Instability** below for more details on design stability properties]. The biggest downside of using DT as an ablator, as demonstrated in OMEGA experiments, is the low absorption fraction caused by inverse bremsstrahlung and low threshold for the two-plasmon-decay (TPD) instability,[14] which generates suprathermal electrons that preheat the fuel. Currently, there is no experimental demonstration of low-adiabat, high fuel compression in direct-drive designs with DT or D_2 ablators driven at ignition-relevant intensities above 5×10^{14} W/cm^2 (this will be discussed further in **Cryogenic D_2 Implosions on the OMEGA Upgrade Laser System from 2001 Until Mid-2008**, p. 85). In the design presented in Fig. 130.17, the fuel is accelerated by 1.5 MJ of laser energy to a peak velocity of $V_{\mathrm{imp}} = 4.3 \times 10^7$ cm/s at adiabat $\alpha = 3$. The target ignites and gives a 1-D gain of 45 with an ITF of 5. This design uses a continuous pulse shape (as opposed to the picket pulse described in the next section), launching the initial shock that sets the in-flight shell adiabat. Later, at $t = 4$ ns, the intensity gradually rises, launching a compression wave. The head of this wave catches up with the first shock in the vapor region, soon after it breaks out of the shell. Timing the first shock and compression wave breaking out of the fuel and preventing the compression wave from turning into a shock inside the fuel are crucial to achieving ignition in this design.

2. Target Stability Properties: Rayleigh–Taylor Instability Growth and Target IFAR

A shell kinetic energy required to ignite DT fuel in an ICF implosion is strongly dependent on the maximum shell velocity. According to Eq. (1), increasing the shell's velocity to well above the minimum value of $V_{\mathrm{imp}} \sim 3 \times 10^7$ cm/s is beneficial for reducing the laser-energy requirement. Increasing implosion velocity, however, must be achieved without compromising the the shell's integrity due to hydrodynamic instability growth.

To understand how V_{imp} scales with target parameters, we start by writing

$$V_{\mathrm{imp}} \sim g t_{\mathrm{accel}}, \tag{31}$$

where g is shell acceleration and t_{accel} is the acceleration time. The acceleration is determined from Newton's law,

$$M_{\mathrm{shell}}\, g \sim 4\pi R^2 p_a \longrightarrow g \sim 4\pi \frac{p_a R^2}{M_{\mathrm{shell}}}, \tag{32}$$

where M_{shell} is the initial shell mass, R is shell radius, and p_a is ablation pressure. The acceleration time for a given laser energy E_{laser} and drive intensity I is

$$t_{\mathrm{accel}} \sim \frac{E_{\mathrm{laser}}}{4\pi R^2 I}. \tag{33}$$

Substituting Eqs. (32) and (33) into Eq. (31) gives

$$V_{\mathrm{imp}} \sim p_a E_{\mathrm{laser}} \big/ M_{\mathrm{shell}} I.$$

Results of simulations lead to a numerical factor of 0.8 in the latter equation. Therefore,

$$V_{\mathrm{imp}} \simeq 0.8 \frac{p_a E_{\mathrm{laser}}}{M_{\mathrm{shell}} I}. \tag{34}$$

Since $p_a \sim I^{0.8}$ to $I^{0.7}$ (Refs. 1 and 2), implosion velocity increases, for a given shell mass and laser energy, by reducing drive intensity. This intuitively contradictory result can be explained by noting that a lower laser drive is overcompensated by the duration of the shell's acceleration, as shown in Eq. (33). The acceleration distance is longer for lower-intensity drives: $R \sim V_{\mathrm{imp}} t_{\mathrm{accel}} \sim p_a E_{\mathrm{laser}}^2 \big/ M_{\mathrm{shell}} I^2 R^2$, so $R^3 \sim p_a E_{\mathrm{laser}}^2 \big/ M_{\mathrm{shell}} I^2 \sim I^{-1.2}$. The implosion velocity can also be increased, according to Eq. (34), by reducing shell mass. An increase in V_{imp}, however, is beneficial for reducing $E_{\mathrm{k,min}}$ only up to the point where multidimensional effects (asymmetry growth) start to affect target performance. Hydrodynamic instabilities put severe constraints on target designs, limiting the values of the shell mass and adiabat used in a robust target design. To determine such constraints, we next identify target parameters that affect the target stability.

a. Rayleigh–Taylor instability. The dominant hydrodynamic instability in an ICF implosion is the Rayleigh–Taylor (RT) instability.[1,2] The RT instability develops in systems where the heavier fluid is accelerated by the lighter fluid.[15] In an ICF implosion, the heavier shell material is accelerated by the lighter blowoff plasma, creating the condition for RT instability. This instability amplifies shell distortions, seeded by both the ablator and ice roughness, and laser illumination nonuniformities (laser "imprint"[13]). Excessive growth of these perturbations leads to shell breakup during acceleration, limiting the final compression and hot-spot temperature. An example of a direct-drive implosion simulation is shown in Fig. 130.18. Shell distortions developed due to the RT instability during
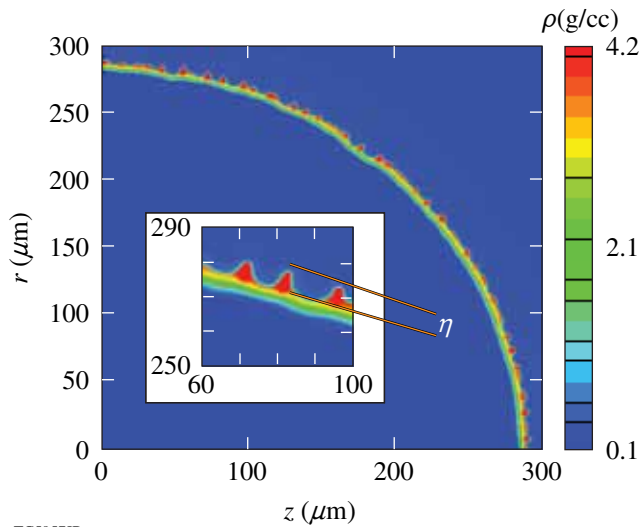
TC5957JR

Figure 130.18
Two-dimensional simulation of a direct-drive implosion using the hydrocode *DRACO*. Rayleigh–Taylor instability causes shell distortions with amplitude η to grow in time.

acceleration are clearly visible in this simulation. The small initial perturbation amplitude η_0 grows in time as

$$\eta \sim \eta_0 e^{\gamma_{RT} t}, \tag{35}$$

where γ_{RT} is the growth rate. In the classical RT configuration where a heavier fluid with density ρ_2 is supported by a lighter fluid of density ρ_1 in a gravitational field g directed from heavier to lighter fluids, the RT growth rate is[15]

$$\gamma_{RT,classical} = \sqrt{A_T k g}, \quad A_T = \frac{\rho_2 - \rho_1}{\rho_2 + \rho_1}, \tag{36}$$

where A_T is Atwood number, $k = 2\pi/\lambda$ is the perturbation wave number, and λ is the perturbation wavelength. In an ICF implosion, the thermal conduction (electron dominant in direct-drive implosions and x-ray radiation dominant in indirect-drive implosions) that drives the ablation process significantly reduces the growth rate from its classical value.[16] The full expression for the growth rate in this case is rather complicated and can be found in Ref. 17. Here, we show the growth rate in the limit $kL_0 < 1$, where L_0 is the effective thickness of the ablation front,

$$\gamma_{RT,ICF} \simeq \sqrt{kg - \Omega_{bl}^2 + \Omega_a^2} - \Omega_a,$$
$$\Omega_{bl} = k\sqrt{V_a V_{bl}}, \tag{37}$$
$$\Omega_a = 2kV_a,$$

where V_a and V_{bl} are the ablation and blowoff velocities, respectively (for the definition of V_{bl}, see Ref. 17). Because mass density in the plasma blowoff region is much smaller than shell density, $A_T \simeq 1$ for modes with $kL_0 < 1$. There are two stabilizing terms in $\gamma_{RT,ICF}$: the first is proportional to Ω_{bl} and the other to Ω_a. Both of them are due to the mass ablation driven by thermal conduction; physical mechanisms of the two, however, are different.

The ablation process is characterized by the ablation velocity V_a, defined as the ratio of the mass ablation rate per unit area of target surface, $(dM/dt)/(4\pi R^2)$, and the shell density at the ablation front $\rho_{shell,abl}$ (see Fig. 130.19),

$$V_a = \frac{dM}{dt} \Big/ \left(4\pi R^2 \rho_{shell,abl}\right), \tag{38}$$

where R is the ablation-front radius. When mass ablation is included, several physical mechanisms reduce the ablation-front perturbation growth and, in some cases, totally suppress it. These are illustrated in Fig. 130.20. First, different plasma blowoff velocities at different parts of the corrugated ablation region create modulation in the dynamic pressure or "rocket effect" that leads to a stabilizing restoring force.[13,18,19] Indeed,
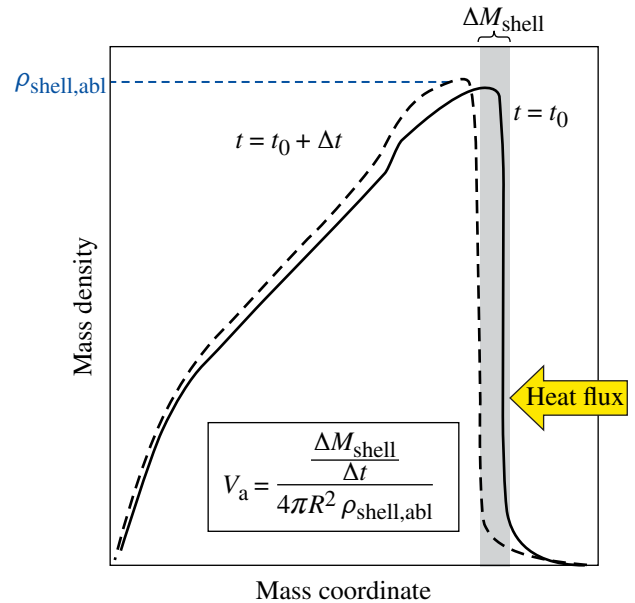
TC9995JR

Figure 130.19
Ablation velocity is defined as mass ablation rate, $\Delta M/\Delta t \simeq dM/dt$, divided by the ablation region surface area $4\pi R^2$ and the shell density at the ablation front $\rho_{shell,abl}$.
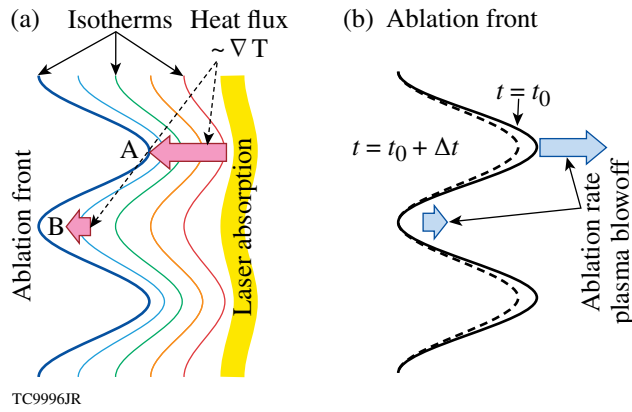
Figure 130.20
(a) Ablation-front modulation creates stronger temperature gradients at perturbation peaks (A) and weaker gradients at valleys (B). Since heat flux is proportional to such gradients, this leads to a slightly enhanced heat flux at A and a reduced heat flux at B. (b) Modulation in heat flux results in modulation in the mass ablation rate. The mass removed by ablation at point A is larger than that at point B, leading to both a fire-polishing effect and a restoring force caused by dynamic overpressure.

as a result of the perturbation growth, the peaks [point A in Fig. 130.20(a)] of the ablation-front ripple protrude into the hotter plasma corona, and the valleys [point B in Fig. 130.20(a)] recede toward the colder shell material. Since the temperature is uniform along the ablation front,[16] the temperature gradients and the heat fluxes are slightly enhanced at the peaks and reduced at the valleys, as shown in Fig. 130.20(a). An excess/deficiency in the heat flux speeds up/slows down the ablation front. This is illustrated in Fig. 130.20(b), where the solid and dashed lines indicate the positions of the ablation front at two instances in time separated by Δt. The ablation front at the peaks (point A) propagates further into the shell than at the valleys (point B). This increases velocity of the blowoff material ("exhaust" velocity, if an analogy of the ablatively driven shell with a rocket is used) at point A and reduces it at point B. A modulation in the blowoff velocity leads to a modulation in the dynamic pressure, creating a restoring force and reducing perturbation growth [see terms with Ω_{bl}^2 in Eq. (37)]. The second stabilizing mechanism caused by ablation is an increased mass ablation rate at the perturbation peaks in comparison with the valley. This leads to faster mass removal at point A and slower removal at point B (so-called "fire-polishing" effect). The latter effect gives the stabilizing terms proportional to Ω_a in Eq. (37).

Since the ablation and blowoff velocities are inversely proportional to the shell density at the ablation front, and density and ablation pressure are related as $\rho_{shell,abl} \sim \left(p_a / \alpha_{abl}\right)^{3/5}$, the velocities scale with the adiabat near the ablation front α_{abl} as

$$V_a \sim V_{bl} \sim \alpha_{abl}^{3/5}. \tag{39}$$

Equation (39) shows that reducing shell density or increasing shell adiabat at the ablation front enhances shell stability.

b. Target in-flight aspect ratio (IFAR). The other important parameter characterizing shell stability is the shell's in-flight aspect ratio (IFAR) defined as the ratio of the shell's radius R to the in-flight shell thickness $\Delta_{in\,flight}$ (see Fig. 130.21). Designs with thicker shells are less sensitive to the instability growth because they break up at a larger distortion amplitude and have smaller seeding of the deceleration RT instability. Such an instability develops as lower-density vapor pushes against the higher-density shell. During the shell acceleration, perturbations feed through from the unstable ablation front to the inner shell $\eta_{inner} \sim \eta_{ablation} e^{-k\Delta_{in\,flight}}$. As the shell decelerates, the inner surface distortions start to grow from η_{inner}, leading to hot-spot deformation at peak compression. Therefore, the thicker the shell, the smaller the feedthrough factor, and the smaller the finite hot-spot deformation.
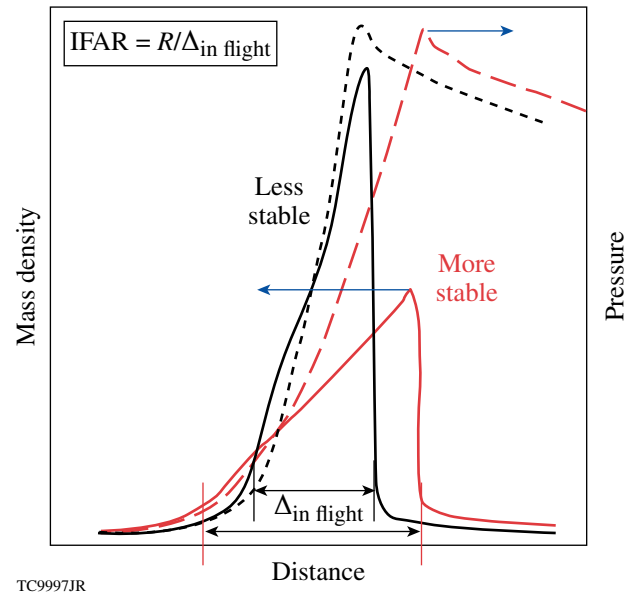

Figure 130.21
In-flight aspect ratio is defined as the ratio of the shell's radius to the in-flight shell thickness. Designs with smaller IFAR are less sensitive to the shell's distortion growth since they break up at larger distortion amplitudes.

Next, we find a scaling of IFAR with implosion parameters. As defined, IFAR = $R/\Delta_{in\,flight}$. The in-flight shell thickness is the initial shell thickness Δ_0 reduced by shell compression during acceleration (effect of mass ablation is neglected in this analysis),

$$\Delta_{\text{in flight}} \simeq \Delta_0 \frac{\rho_0}{\langle\rho\rangle_{\text{in flight}}} \frac{R_0^2}{R^2}, \tag{40}$$

where ρ_0 and $\langle\rho\rangle$ are initial and average in-flight shell densities, respectively, and R_0 is the initial shell radius. For the all-DT design where the shell consists mainly of DT, $\langle\rho\rangle_{\text{in flight}} = \left[p_a(\text{Mbar})\big/2.2\langle\alpha\rangle\right]^{3/5}$, where $\langle\alpha\rangle$ is the mass-averaged shell adiabat. This gives

$$\text{IFAR} = \frac{R}{\Delta_{\text{in flight}}}$$

$$\simeq 10\frac{R_0}{\rho_0\Delta_0}\left(\frac{R}{R_0}\right)^3\left(\frac{p_a}{100\ \text{Mbar}}\right)^{3/5}\langle\alpha\rangle^{-3/5}. \tag{41}$$

Multiplying the numerator and denominator of Eq. (41) by $4\pi R_0^2$ and replacing $4\pi R_0^2\Delta_0\rho_0$ with the shell mass M_{shell} yields

$$\text{IFAR} = 10\left(\frac{4\pi R_0^3}{M_{\text{shell}}}\right)\left(\frac{R}{R_0}\right)^3\left(\frac{p_a}{100\ \text{Mbar}}\right)^{3/5}\langle\alpha\rangle^{-3.5}. \tag{41a}$$

Initial shell radius in an optimized design is proportional to shell's velocity times acceleration time, $R_0 \sim V_{\text{imp}}t_{\text{accel}}$ and the required shell mass is given by Newton's law $MR_0\big/t_{\text{accel}}^2 \sim 4\pi p_a R_0^2$. Eliminating t_{accel} from the latter two equations gives

$$\frac{4\pi R_0^3}{M} = \frac{V^2}{p_a}. \tag{42}$$

Combining Eqs. (41a) and (42) leads to

$$\text{IFAR} = 90\frac{R^3}{R_0^3}\left(\frac{V_{\text{imp}}}{3\times10^7}\right)^2\left(\frac{p_a}{100\ \text{Mbar}}\right)^{-2/5}\langle\alpha\rangle^{-3/5}. \tag{43}$$

Equation (43) shows that IFAR's value decreases as the shell implodes (the ratio R/R_0 gets smaller), reaching its peak value at the beginning of the shell's acceleration, when drive intensity reaches its peak value. Then, the stability property of a design is characterized by this peak IFAR value. Fit to the results of numerical simulations gives[20]

$$\max(\text{IFAR}) \simeq 60\left(\frac{V_{\text{imp}}}{3\times10^7}\right)^2\left(\frac{p_a}{100\ \text{Mbar}}\right)^{-2/5}\langle\alpha\rangle^{-3/5}, \tag{44}$$

which can be recovered from Eq. (43) by using $R \simeq 0.9R_0$. Numerical simulations of directly driven cryogenic implosions (both on OMEGA and the NIF) show that to keep the shell from breaking up because of the short-scale perturbation growth during the acceleration, IFAR should not exceed

$$\text{IFAR}_{\text{max}} \simeq 40. \tag{45}$$

Using Eq. (44), we conclude that increasing implosion velocity by reducing the drive intensity alone, as Eq. (34) suggests, is not the best strategy from a stability point of view since two factors cause IFAR in this case to increase: (1) an increase in V_{imp} and (2) a reduction in p_a. The fact that reduction in drive pressure increases IFAR is a consequence of the larger traveled distances required to accelerate a shell to a given V_{imp} if the drive pressure is lower. Larger acceleration distances mean larger initial shell radius and higher IFAR. This is illustrated in Fig. 130.22, where initial shell dimensions are schematically shown for different drive intensities. The smallest drive intensity requires the largest initial and in-flight aspect ratios.

Increasing the implosion velocity by reducing shell mass has a lesser effect on IFAR since the latter increases only as a
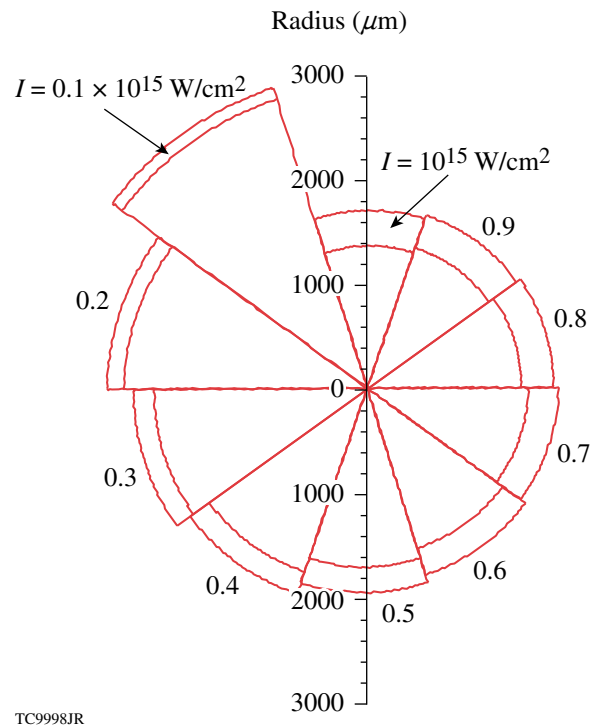

TC9998JR

Figure 130.22
Initial shell dimensions for all-DT designs driven at indicated intensities using $E_{\text{laser}} = 1.5$ MJ.

result of larger V_{imp} [see Eq. (43)]. This approach, however, has limited beneficial effects: As the IFAR exceeds the maximum value set by the stability considerations, the target performance begins to degrade. Improving shell stability while reducing shell mass can be accomplished, according to Eq. (44), by increasing the average shell adiabat $\langle \alpha \rangle$. This must be done, however, without raising the adiabat of the unablated fuel since that is set by the condition on maximum fuel pressure at stagnation, as shown in Eq. (25). An adiabat-shaping technique[21] was proposed and implemented in the direct-drive designs to raise the adiabat only at the outer part of the shell, without degrading the adiabat at the inner part of the fuel. The designs with adiabat shaping will be discussed in **Cryogenic D$_2$ Implosions on the OMEGA Upgrade Laser System from 2001 Until Mid-2008**, p. 85).

Experimental Cryogenic Program on OMEGA

The experimental cryogenic program on OMEGA is designed to study fundamental physics of direct-drive ICF implosions. In particular, the following key questions are addressed:

(1) Is a low-adiabat compression of cryogenic fuel possible in a spherical implosion driven by direct laser illumination?

(2) Can cryogenic fuel be accelerated to velocities in excess of 3×10^7 cm/s in such implosions?

(3) At what drive intensities does the laser drive become inefficient in accelerating low-adiabat fuel, creating an excessive amount of fuel preheat because of suprathermal electrons, and scattering a significant fraction of the incident laser light as a result of laser–plasma interaction?

(4) Can asymmetry growth be controlled during an implosion, so

　(a) the short-scale perturbations with wavelength $\lambda \sim \Delta_{in\ flight}$ do not compromise shell integrity, and

　(b) hot-spot deformation is not severe enough to significantly reduce hot-spot ion temperature and quench the yield?

To answer these questions, various experimental techniques were developed and used to diagnose OMEGA implosions. Selecting a specific technique is based on measurement accuracy, which must be high enough to be able to tune the physics models and to meet the predictive accuracy goals discussed in

Sensitivity of Ignition Condition on Implosion Parameters (p. 75). Next, we list the experimental techniques that are used to address these key questions.

1. Adiabat

The shell adiabat during an implosion can be inferred from shell density and temperature measurements. Two techniques have been developed and used on OMEGA implosions to measure these quantities: spectrally resolved x-ray scattering[22,23] and time-resolved x-ray absorption spectroscopy.[24] X-ray scattering requires large scattering volumes to keep signal-to-noise ratio at acceptable levels. This significantly limits the accuracy of measuring the adiabat at inner parts of the shells in designs with spatial adiabat gradients. The x-ray absorption technique, on the other hand, is designed to be much more local since the temperature and density are inferred by analyzing the spectral shapes of a backlighter source attenuated by a buried mid-Z tracer layer inside the shell. Hydrodynamic instabilities developed during shell implosion, however, redistribute the signature layer material throughout the shell, making temperature and density measurements dependent on the accuracy of mix models.

A significant progress in understanding how to infer the fuel adiabat in a spherical implosion was made after Ref. 21 demonstrated that the peak in areal density in an optimized implosion depends mainly on laser energy and the average adiabat of the unablated mass,

$$\max(\rho R)_{optimized} \simeq 2.6 \frac{\left[E_{laser}(MJ)\right]^{1/3}}{\alpha^{0.54}}. \qquad (46)$$

This scaling can be understood based on the following consideration: The unablated mass at the beginning of shell deceleration can be written as

$$M \sim \rho_d \Delta_d R_d^2, \qquad (47)$$

where $\Delta_d = R_d / A_d$ is the shell thickness and A_d is the shell aspect ratio at the start of shell deceleration, respectively. The mass is related to drive pressure (or shell pressure at the beginning of deceleration, p_d) using Newton's law,

$$M \frac{R_d}{t_{accel}^2} \sim p_d R_d^2 \longrightarrow M \sim p_d R_d t_{accel}^2, \qquad (48)$$

where t_{accel} is defined in Eq. (33). Equating the right-hand sides of Eqs. (47) and (48) yields

$$R_d \sim t_{\mathrm{accel}} \sqrt{\frac{p_d}{\rho_d} A_d} \sim \left(\frac{E_{\mathrm{laser}}}{V_{\mathrm{imp}}^2 I}\right)^{1/3} \sqrt{\frac{p_d}{\rho_d} A_d}. \qquad (49)$$

At peak compression, the main contribution to areal density is given by the shock-compressed region. Therefore, rewriting Eq. (14) as

$$M_{\mathrm{eff}} \sim (\rho\Delta)_{\mathrm{shocked}} R^2 \sim \rho_d R_d^2 \frac{R}{R_d} \qquad (50)$$

leads to

$$\max(\rho R) \sim (\rho\Delta)_{\mathrm{shocked}} \sim \rho_d R_d \left(\frac{R_d}{R}\right). \qquad (51)$$

Substituting Eqs. (49) and (13) into Eq. (51) results in

$$\max(\rho R) \sim p_d \left(\frac{\rho_d}{p_d}\right)^{5/6} \frac{E_{\mathrm{laser}}^{1/3}}{I^{1/3}} \sqrt{A_d}. \qquad (52)$$

Finally, replacing ρ_d with $\sim (p_a/\alpha)^{3/5}$

$$\max(\rho R) \sim \frac{p_d^{2/3}}{I^{1/3}} \sqrt{A_d} \frac{E_{\mathrm{laser}}^{1/3}}{\sqrt{\alpha}}. \qquad (53)$$

Shell aspect ratio at the start of the deceleration phase has a weak dependence on implosion parameters: For an implosion with a higher shell adiabat, the shell is thicker but the deceleration phase starts while the shell is at larger radius, so the ratio R_d/Δ_d is approximately a constant $A_d \simeq 2$ for all implosion

conditions. For a well-tuned implosion when the drive pressure keeps pushing the shell up to the beginning of shell deceleration (shell coasting is minimized), $p_d \sim p_a$. Since $p_a \sim I^{2/3}$, Eq. (53) becomes

$$\max(\rho R)_{\mathrm{optimized}} \sim I^{1/9} \sqrt{A_d} \frac{E_{\mathrm{laser}}^{1/3}}{\sqrt{\alpha}}, \qquad (54)$$

which agrees with the numerical fit shown in Eq. (46), taking into account the weak dependence of $\sqrt{A_d}\, I^{1/9}$ on implosion parameters. When ablation drive is terminated early and the shell starts to decompress during the coasting phase, p_d drops, reducing the maximum areal density [see Eq. (53)].

Equation (53) shows that the adiabat of an unablated mass in an implosion without a significant coasting phase can be inferred by measuring the areal density close to the shell's peak convergence. The areal density in an ICF implosion is measured using either x-ray backlighting,[25] Compton radiography,[26] or charged-particle spectrometry.[27,28] While the first two techniques are still under development, the areal density in current cryogenic experiments is inferred by measuring the spectral shapes of fusion-reaction products. Areal density in D_2 fuel is determined from energy downshift in secondary protons[27] created in D–^{3}He reactions [primary reaction creates a neutron and ^{3}He ion, $D + D \longrightarrow n(2.45\ \mathrm{MeV}) + {}^3\mathrm{He}\ (0.82\ \mathrm{MeV})$, and a secondary reaction creates an α particle and a proton, $^3\mathrm{He} + D \longrightarrow \alpha\ (6.6\text{–}1.7\ \mathrm{MeV}) + p\ (12.6\text{–}17.5\ \mathrm{MeV})$]. This is shown in Fig. 130.23.
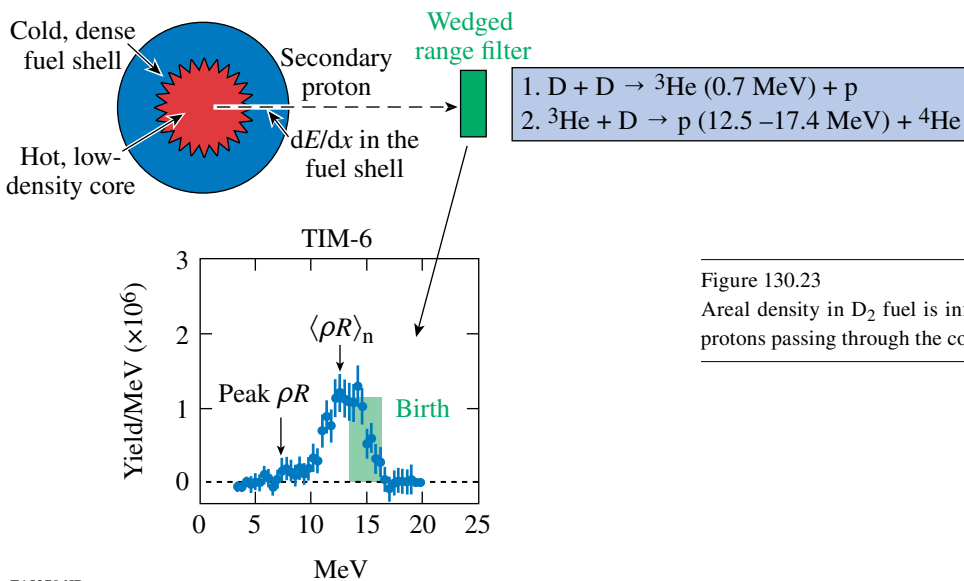

Figure 130.23
Areal density in D_2 fuel is inferred from energy attenuation of secondary protons passing through the cold shell material.

E15270dJR

For DT fuel, the areal density is inferred by using a magnetic recoil spectrometer (see Fig. 130.24) that measures the fraction of neutrons down-scattered from fuel deuterons and tritons[28] (this fraction is directly proportional to the fuel ρR).

The main advantage to using charged-particle spectrometry to measure areal densities is that the peak in the reaction rate and peak fuel compression are not far apart (for OMEGA implosions they are separated by 20 to 30 ps with the peak in neutron production being earlier), so the reaction products sample areal density close to its peak value. The fusion rates are affected, on the other hand, by the nonuniformity growth that reduces both the fuel ion temperature and fuel "clean" volume where reactions take place. This changes timing and sampling of areal density by fusion-reaction products. The sensitivity of areal density measurement to neutron-production timing can be shown by noting that areal density evolves on a time scale $\Delta t_{\rho R} \sim 2\Delta t$, where Δt is the confinement time defined in Eq. (9). For OMEGA-scale targets this gives

$$\Delta t_{\rho R} \sim 2\frac{R}{V_{\text{imp}}} \sim 2\frac{2 \times 10^{-3}\ \text{cm}}{3 \times 10^{7}\ \text{cm/s}} \simeq 130\ \text{ps},\qquad (55)$$

while the temporal width of neutron production in a spherically symmetric implosion is twice less,

$$\Delta t_{\text{n}} \simeq \Delta t \simeq 70\ \text{ps}.\qquad (56)$$

The areal density and neutron production histories for a typical cryogenic-DT target are shown in Fig. 130.25. Since the temporal scale of ρR evolution is short, the effect of perturbation growth on neutron-production timing and duration must be taken into account when comparing the experimentally inferred ρR values with the predictions.
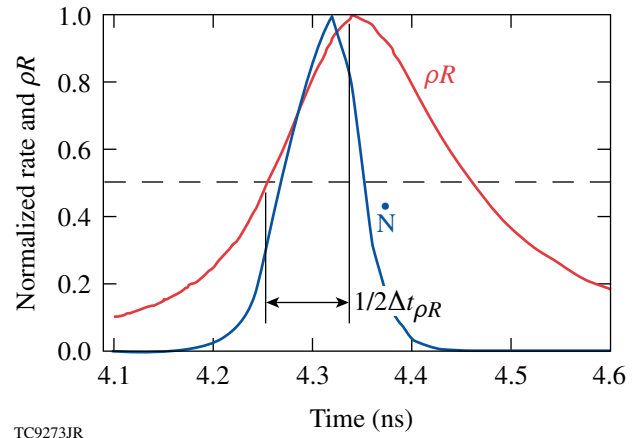

TC9273JR

Figure 130.25
Areal density and neutron-production–rate evolution for a typical cryogenic implosion on OMEGA.
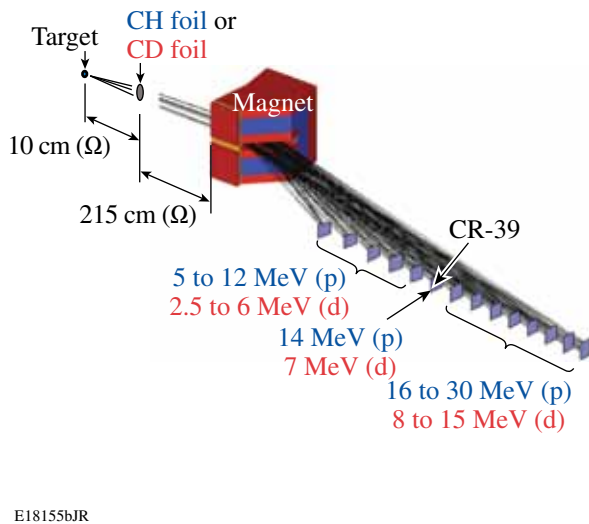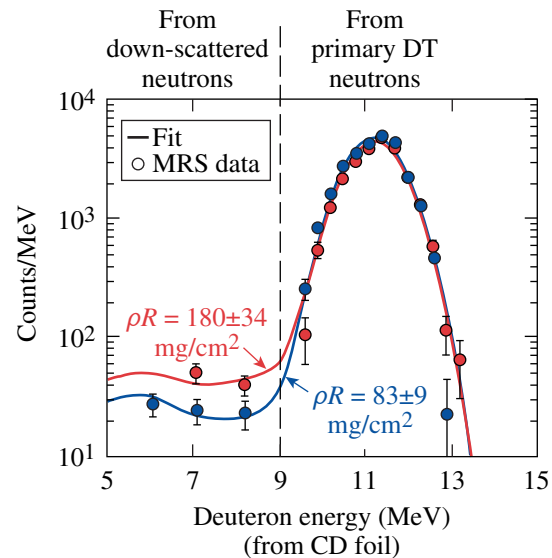

E18155bJR

Figure 130.24
Areal density in DT fuel is inferred from measurements of the down-scattered fraction of primary neutrons produced in a D + T reaction.

2. Implosion Velocity

Implosion velocity is the key parameter that determines how much kinetic energy the fuel must acquire to ignite [see Eq. (1)]. Shell velocity can be inferred from trajectory measurements using either time-resolved x-ray–backlit images[29] of an imploding shell or time-resolved self-emission images.[25,30] The most-accurate measurement (although indirect) of hydrocoupling efficiency in implosions on OMEGA is done by measuring the onset of neutron production. Temporal history of the neutron rate is measured on OMEGA using neutron temporal diagnostics (NTD).[31] The absolute timing of NTD is calibrated to better than ±50 ps, which is equivalent to a spread in the implosion velocity of ±3.5% for OMEGA-scale targets. Figure 130.26 illustrates the sensitivity of neutron-production timing to the variation in shell velocity. Here, the shell velocity (dashed lines) and neutron rate (solid lines) histories are calculated using two different laser-deposition models. The implosion velocity predicted with the less-efficient drive (red lines) is 5% lower than that predicted for higher-efficiency drive (blue lines), resulting in a 200-ps delay in neutron production. Such a delay is easily observed in an experiment since this time difference is well outside the measurement error bar.
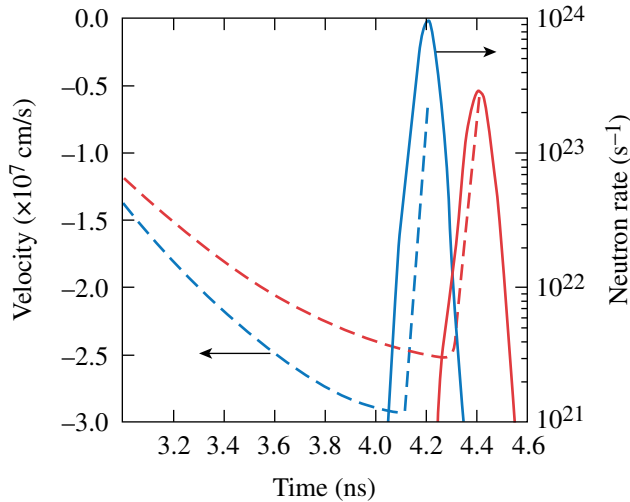
TC9999JR

Figure 130.26
Shell velocity (left axis, dashed lines) and neutron production rates (right axis, solid lines) calculated for an OMEGA cryogenic design using two different laser-deposition models. The less-efficient laser absorption (red lines) predicts smaller shell velocity and later neutron-production timing.

3. Ion Temperature at Time of Peak Neutron Production

The fuel ion temperature at peak neutron production depends on the shell's kinetic energy during the acceleration phase of implosion and on the growth of the hot-spot distortions while the shell decelerates. The ion temperature in an implosion is inferred by measuring the temporal width of the primary-neutron signal.[32] The thermal broadening of the neutron energy distribution ΔE_{FWHM} is related to the local ion temperature T_i as[33]

$$\Delta E_{\mathrm{FWHM}} = 177\sqrt{T_i}, \qquad (57)$$

where both ΔE_{FWHM} and T_i are measured in keV. Then, measuring the neutrons' time of flight (TOF) from the target to a detector, $\mathrm{TOF} = 72.3\, L/\sqrt{E_n}$, the neutron-averaged ion temperature is inferred relating TOF broadening Δ_{TOF} with ΔE and using Eq. (57),

$$\langle T_i \rangle_{n,\exp} = 68 \frac{\Delta_{\mathrm{TOF}}^2}{L^2}, \qquad (58)$$

where L is the distance from detector to target in meters, $E_n = 14.1$ is the energy (in MeV) of primary neutrons in the D + T reaction, and TOF is measured in nanoseconds. Strictly speaking, the neutron spectral width is determined not only by thermal broadening, but also by gradients in the bulk fluid velocity of the reacting fuel. The latter contribution is not very important in a spherically symmetric implosion since the peak in neutron production occurs while the fuel is close to stagnation. When drive and target nonuniformities are taken into account, however, fuel flow caused by asymmetry growth can make a significant contribution to neutron spectral width. Therefore, comparing $\langle T_i \rangle_{n,\exp}$ with calculations, the bulk fluid motion must be taken into account in this case. To generalize Eq. (57), including the effect of bulk motion, we start with Eq. (29) of Ref. 33 and write the neutron kinetic energy as

$$E_n \simeq \frac{m_\alpha}{m_n + m_\alpha} Q + (\mathbf{V} \cdot \mathbf{e}_n)\sqrt{\frac{2 m_n m_\alpha Q}{m_n + m_\alpha}}, \qquad (59)$$

where Q is nuclear energy released in a fusion reaction ($Q = 17.6$ MeV for D + T reaction), m_n and m are masses of reaction products (neutron and alpha-particle mass, respectively, for DT), $\mathbf{V}$ is the velocity of the center of mass of reaction products, and $\mathbf{e}_n$ is a unit vector in the direction of neutron velocity (and direction to a neutron detector). If $\mathbf{V}_f$ is the fluid velocity, then averaging over thermal motion gives

$$\langle E_n \rangle \simeq E_0 + V_f \cos\theta_n \sqrt{2 m_n E_0}, \qquad (60)$$

where $E_0 = m_\alpha/(m_n + m_\alpha) Q$ ($E_0 = 14.1$ MeV for DT), and θ_n is the angle between fluid flow and neutron velocity. Next, using Eq. (36) of Ref. 33, the neutron distribution at a particular location in a plasma with ion temperature T_i becomes

$$f_n(E) = e^{-\left(\frac{E-E_0}{\Delta E} - M_a \cos\theta_n\right)^2}, \quad \Delta E = 2\sqrt{\frac{m_n T_i E_0}{m_n + m_\alpha}}, \quad (61)$$

where $M_a = V_f / c_s$ is the flow Mach number $c_s = \sqrt{T_i / m_i}$ is the ion sound speed, and $m_i = (m_n + m_\alpha)/2$ is the average fuel ion mass. According to Eq. (61), a fluid velocity, uniform in the direction of the neutron detector, affects only the position in the peak of the distribution function, but not its width. Averaging the distribution function over the fuel volume gives

$$\langle f_n(E)\rangle_V = \frac{\int dV n^2 \langle\sigma\nu\rangle e^{-[\alpha(E)-M_a\mu]^2}}{\int dV n^2 \langle\sigma\nu\rangle}, \quad (62)$$

where $\mu = \cos\theta$, $\langle\sigma\nu\rangle$ is reaction cross section, n is ion density, $\alpha(E) = (E - E_0)/\Delta E$. Taking the integral over the angles assuming spherical symmetry in Eq. (62) yields

$$\langle f_n(E)\rangle_V =$$

$$\sqrt{\pi} \frac{\int_0^R dr\, r^2 n^2 \langle\sigma\nu\rangle \{\mathrm{erf}[\alpha(E)+M_a] - \mathrm{erf}[\alpha(E)-M_a]\}}{4 M_a \int_0^R dr\, r^2 n^2 \langle\sigma\nu\rangle}, \quad (63)$$

where erf is the error function. Integrating Eq. (63) over the neutron-production time and fitting the result with a Gaussian with FWHM = ΔE_{fit},

$$\int dt \langle f_n(E)\rangle_V \xrightarrow{\text{fit}} \exp\left[-4\ln 2\left(\frac{E-E_0}{\Delta E_{\mathrm{fit}}}\right)^2\right],$$

defines an effective temperature $\langle T_i\rangle_{n,\mathrm{fit}} = (\Delta E_{\mathrm{fit}}/177)^2$ to be compared with the measurements [see Eq. (58)]. A bulk flow with velocity distribution not pointing in the same direction broadens the neutron spectrum, leading to a higher effective ion temperature. This is illustrated by evaluating the angular integral in Eq. (62), assuming $M_a \ll 1$ and spherical symmetry,

$$\frac{1}{2}\int_{-1}^{1} d\mu\, e^{-\alpha^2 + 2\alpha M_a \mu} \simeq \frac{e^{-\alpha^2}}{2}\int_{-1}^{1} d\mu\left[1 + 2(\alpha M_a)^2 \mu^2\right]$$

$$\simeq e^{-\alpha^2/\left(1 + 2M_a^2/3\right)}. \quad (64)$$

Equation (64) gives

$$\langle T_i\rangle_{\mathrm{fit}} = T_i\left(1 + \frac{2}{3}M_a^2\right) = T_i + \frac{2}{3}m_i V_f^2.$$

For a spherically symmetric flow, $\langle T_i\rangle_{\mathrm{fit}}$ tracks T_i within a few percent since the fuel is close to stagnation at the neutron-production time. When significant asymmetries are present, bulk flow can lead to a significant contribution to $\langle T_i\rangle_{\mathrm{fit}}$, making an inferred ion temperature larger than the actual thermodynamic value.

Early Experiments on the OMEGA-24 Laser

The first experiments with layered DT targets were performed on the OMEGA-24 Laser System[34] in the late 1980s (Refs. 35 and 36). The targets were spherical 3- to 5-μm-thick glass shells with outer radii of 100 to 150 μm. The cryogenic, 5- to 10-μm-thick solid DT layers were produced using a fast-freeze technique.[37] These targets were driven with 1 to 1.2 kJ of UV energy delivered with 650-ps Gaussian pulses (with a peak in drive intensity of up to 6×10^{14} W/cm^2). The target and drive pulse are shown in Fig. 130.27(a). The predicted convergence ratios in these implosions were relatively high, $C_r \sim 20$ (C_r is defined as the ratio of the initial to the minimum radius of the fuel–glass interface) with a peak DT density of ~300 g/cm^3 and a peak fuel areal density of 150 mg/cm^2. For comparison, the all-DT ignition design described in **All-DT, Direct-Drive, NIF-Scale Ignition Target Design** (p. 76) has $C_r = 27$. Targets were held inside the U-shaped cradle using three to five spider silks. These early designs were highly susceptible to the RT instability since the peak of the in-flight aspect ratio (IFAR) approached 70, a much higher value than currently considered to be acceptable for a robust design, IFAR < 40 (see **Target In-Flight Aspect Ratio**, p. 79). The areal densities in these experiments were directly measured (the first such measurement performed in an ICF implosion at that time) by counting the down-scattered fraction of deuterium and tritium atoms.[38] Even though the inferred fuel areal density and mass density were the highest measured to date, they were lower than predictions by 40% to 60%. Figure 130.27(b) plots the predicted value of fuel areal density using the 1-D hydrocode *LILAC*[39] and inferred areal densities using knock-on statistics. A significant deviation in the predicted value has occurred for an effective fuel adiabat $\alpha < 4$. This is not surprising considering the high IFAR of these shells. If perturbation growth causes a shell to break up during acceleration, it creates a low-density precursor ahead of the imploding shell, which causes the shell to stagnate at a larger radius with a smaller peak areal density.

Cryogenic D$_2$ Implosions on the OMEGA Upgrade Laser System from 2001 Until Mid-2008

The fast-freezing technique employed to make cryogenic targets on OMEGA-24 could not be used to produce thicker fuel layers required for ignition-relevant OMEGA-scaled designs.
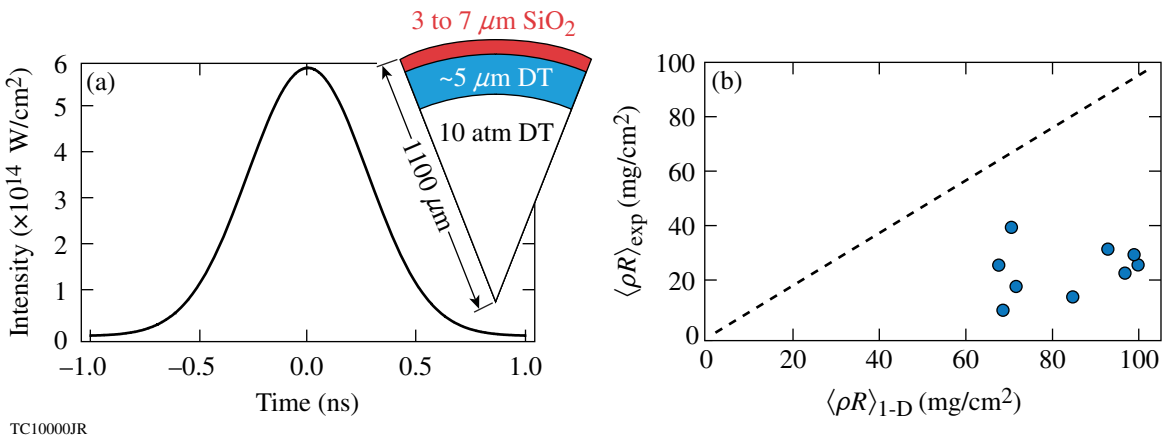
Figure 130.27

(a) Pulse shape and target and (b) predicted and inferred fuel areal densities for cryogenic implosions on the OMEGA-24 Laser System.

Novel techniques for producing smooth DT and D_2 layers were introduced in the 1980s and 1990s. A "β-layering" was demonstrated to make uniform solid DT layers,[40] and IR radiation was shown to produce layer smoothing in cryogenic D_2 fuel by exciting the vibration–rotation band.[41] The newly developed cryogenic system[42] on the OMEGA Upgrade (30 kJ of UV energy, 60-beam system)[43] employed both these techniques for cryogenic target production. Cryogenic experiments on the new system started in 2000 by imploding D_2 targets.[44] DT was introduced in February 2006, after completion of an extensive system readiness review associated with the radiological impact of using tritium.[45] Since target production was on a learning path to improving D_2-layer quality, the first implosions used a square laser drive pulse with laser energy ~23 kJ to set the cryogenic fuel on a high adiabat $\alpha \sim 25$ (see green dashed line in Fig. 130.28). The acceleration phase in this design was very short so the impact of the RT growth on target performance was minimal. The yields, areal densities (30 to 60 mg/cm^2), and timing of neutron production were consistent with 1-D and 2-D hydrocode simulations.[44,46]

As the uniformity of ice layers dramatically improved from $\sigma_{rms} = 9$ to 15 μm down to 1 to 3 μm in 2002, experiments began using designs that approached the OMEGA-scaled version of the all-DT ignition designs.[47] These were 3- to 5-μm-thick CD shells overcoated over 95- to 100-μm-thick D_2 ice layers driven at $I \sim 10^{15}$ W/cm^2 on $\alpha = 4$ adiabat (see dotted line in Fig. 130.28). These shells were somewhat thicker than required for hydrodynamic scaling (<1 μm) since fill time was shorter and overall long-wavelength shell nonuniformities were smaller. By the middle of 2005, a large data set of these implosions was built sufficient to conclude that the measured
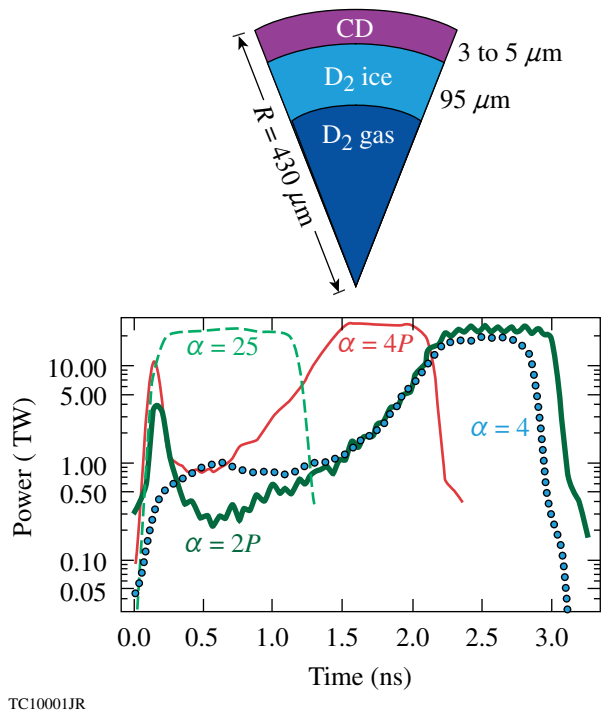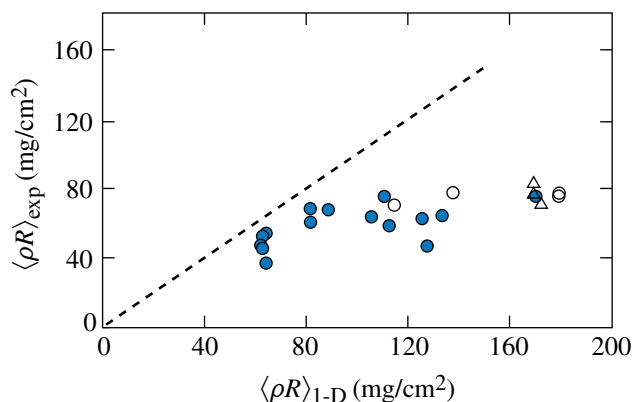

Figure 130.28

Pulse shapes and target for $\alpha = 25$ (dashed), $\alpha = 4$ (red solid and blue dotted lines), and $\alpha = 2$ (thick green line) designs on OMEGA. The designs with the decaying-shock adiabat shaping are shown with solid lines.

areal densities were significantly lower than predicted, as shown with solid circles in Fig. 130.29. For the lowest adiabat (highest ρR) in this series, degradation in areal density was up to 50%, which is equivalent to adiabat degradation [according to Eq. (46)], by up to 70%! The 2-D calculations using the hydrocode *DRACO*[48] and results of the stability postproces-

sor[49] indicated that the shells in the low-adiabat implosions were sufficiently stable (the ratio of the mix width to the shell thickness did not exceed 50%, where the short-scale mix at the ablation front, seeded mainly by laser imprint, was amplified by the RT instability). Measurements of the imprint efficiencies made earlier on planar targets,[50] however, suggested that calculations could be underestimating imprint amplitude as much as by a factor of 2, and the shell in low-adiabat implosions could be broken by the imprint growth. Since shell stability was a main concern at that time, LLE was working on perturbation growth mitigation strategies. A novel technique for reducing the RT growth was proposed in 2002. The idea was to shape the adiabat through the shell (adiabat-shaping designs[20]). This can be accomplished either by launching a shock wave of decaying strength [decaying-shock (DS) design] through the shell[20] or by relaxing the shell material with a short-duration picket and recompressing it later with the shaped main pulse [adiabat shaping by relaxation (RX) design].[51] This sets the outer part of the ablator on a higher adiabat, keeping the inner part of the shell on a lower adiabat. The higher adiabat at the ablation front increases the ablation velocity, mitigating the impact of the RT instability on target performance, as described in **Rayleigh–Taylor Instability**, p. 77.


TC10002JR

Figure 130.29
Measured and predicted areal densities for cryogenic-D_2 implosions using the $\alpha = 4$ pulses shown in Fig. 130.28 (solid circles) and $\alpha = 4P$ (open circles).

Pulse shapes, similar to ones shown in Fig. 130.28 with thin and thick solid lines, were used to implement adiabat-shaping designs on OMEGA. Calculations predicted a significant improvement in shell stability in designs with adiabat shaping in comparison with the original flat-foot designs (see Fig. 130.30). The experiments, however, did not show any significant improvement in measured areal densities, which continued to saturate at ~80 mg/cm². These are shown as open circles in Fig. 130.29. To further support the conclusion that

the short-scale mix caused by the RT growth at the ablation front was not the main contributor to the observed ρR degradation, a series of implosions were performed with an enhanced laser-imprint level by turning off the smoothing by spectral dispersion (SSD).[52] The target yield dropped by a factor of 2 in these implosions, but the areal density remained unchanged (see open triangles in Fig. 130.29).
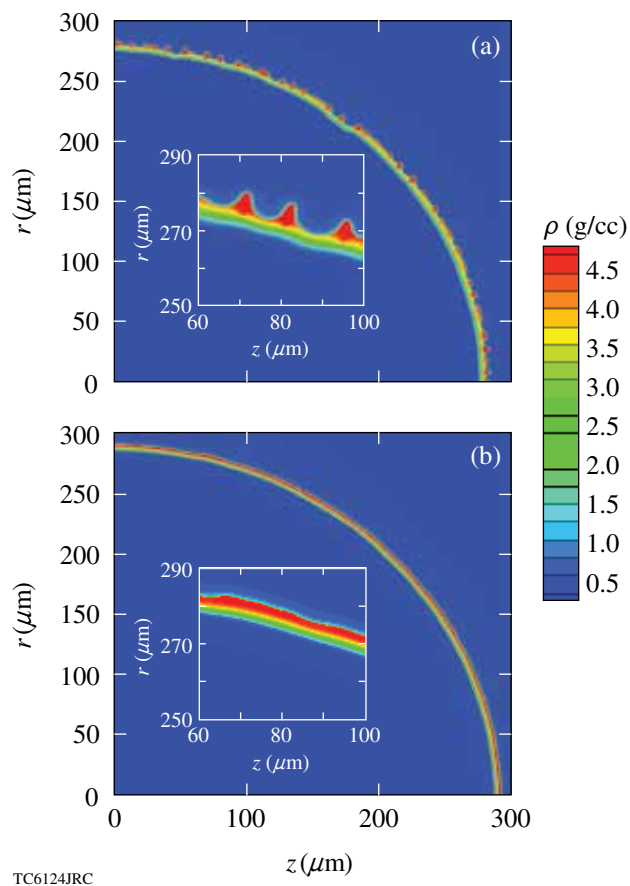
TC6124JRC

Figure 130.30
In-flight shell density contours in designs (a) without and (b) with adiabat shaping.

Since the source of excessive shell heating, not accounted for in a hydrosimulation, was unknown at the time, several scenarios explaining the areal-density deficiency were considered: Excessive shell heating could have been due to (1) suprathermal electrons with $T_{hot} > 40$ keV, (2) radiation, or (3) shock waves. Next, we describe how each of these possibilities were addressed in OMEGA experiments.

1. Suprathermal Electrons
Suprathermal electrons are always present in a plasma because of high-energy tails in the electron distribution function. In addition, laser–plasma interaction processes, such as

two-plasmon-decay (TPD) instability and stimulated Raman scattering (SRS),[53] can generate electrons with energies above 20 keV. These electrons can penetrate the ablator and fuel in OMEGA designs and deposit their energy close to the inner part of the fuel, degrading peak ρR. The electrons in the energetic tails of the distribution function will be addressed first.

a. Electron distribution tails and nonlocal thermal transport. To model electron thermal transport in ICF experiments, a flux-limited model[54] is conventionally used in hydrocode simulations. Thermal conduction in such a model is calculated using the Spitzer expression[55] q_{sp}, which is derived assuming that the electron mean free path is much shorter than the gradient scale-length of hydrodynamic variables.[56] In a narrow region, near the peak of the laser deposition, the temperature profile is steep enough to break the validity condition of the Spitzer formula. The heat flux in this case is calculated as a fraction $f < 1$ of the free-stream conduction $q_{fs} = nTv_T$, where n and T are electron density and temperature, respectively, $v_T = \sqrt{T/m}$ is the electron thermal velocity, and m is electron mass. The limiting factor f is referred to as "flux limiter." The flux-limiter value of $f = 0.06$ is typically used to simulate direct-drive experiments.

Although it was successfully applied to simulate many experimental observables,[57] the flux-limited thermal transport model neglects the effect of finite electron-stopping ranges and cannot be used to access the amount of shell preheat from the energetic electrons in plasma. To account for this effect, a simplified thermal transport model was developed and implemented in the 1-D hydrocode *LILAC*. The model used the Krook-type approximation[58] to the collisional operator to solve the Boltzmann equation without making the high collisionality approximation used in the "classical" Chapman–Enskog method.[56] The modified energy-dependent Krook-type operator[57] conserves particles and energy by renormalizing local electron density and electron temperature (which depend on gradients in hydrodynamic profiles) in the symmetric part of the distribution function (Maxwellian modified to include effects of the laser electric field[59]). When applied to the OMEGA experimental data, the nonlocal model showed no significant inner fuel preheat caused by the energetic electrons in the distribution tail (see Fig. 130.31). These electrons, instead, preheated the ablation front region [see how electron temperature in the calculation using the nonlocal model (thick dashed line in Fig. 130.31) increases toward the ablation front], leading to a greater ablative stabilization of the RT growth. This preheat of the outer region of the shell can explain very little sensitivity of the measured ρR to variation in the source of short-scale perturbations described earlier in this section. Ablation-front

preheating from the nonlocal electrons is also consistent with the short-wavelength stabilization of the RT growth observed in experiments with accelerated planar foils.[60]
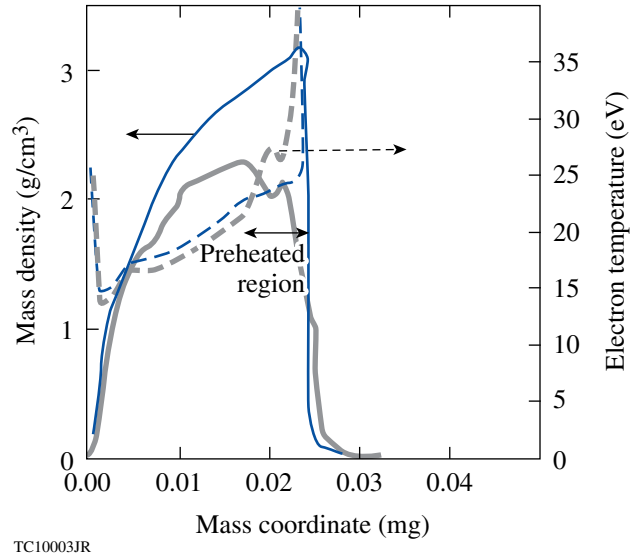

TC10003JR

Figure 130.31
In-flight shell density (solid lines) and electron temperature (dashed) with (thin lines) and without (thick lines) nonlocal effects in electron thermal conduction.

In addition to the ablation region preheating, the strength of the first shock and a compression wave were significantly modified in calculations using the nonlocal electron-transport model.[57] At the beginning of the laser drive, where the hydrodynamic scale lengths are short, the shock strength predicted using the nonlocal model was larger compared to the results of the flux-limited model. This effectively led to shock mistiming and an adiabat degradation prior to the shell acceleration. Experimental validation of the nonlocal model predictions by direct shock-velocity measurement in spherical geometry was not available at that time (the experimental platform was developed in 2008). The existing shock-velocity data in planar geometry, on the other hand, were not very sensitive to differences in predictions using the nonlocal and flux-limited models.[57] Measurements of early-time perturbation evolution (ablative Richtmyer–Meshkov instability[61]), however, clearly indicated that the higher heat fluxes, predicted by the nonlocal model at the beginning of the pulse, are consistent with the observations.[62] In addition, the absorption measurements of Gaussian pulses with FWHM of 200 ps and peak laser intensity varied from 5×10^{13} to 1.2×10^{15} W/cm^2 (Ref. 63) were in much closer agreement with the results of the nonlocal heat-transfer model. These are shown in Fig. 130.32. In addition to the inverse bremsstrahlung, the resonance absorption[53] resulting from tunneling of the laser electric field from the

turning point to the critical surface and exciting plasma waves was included in these simulations.[57,64] The resonant absorption effects were important only early in the pulse when the density scale length is short.
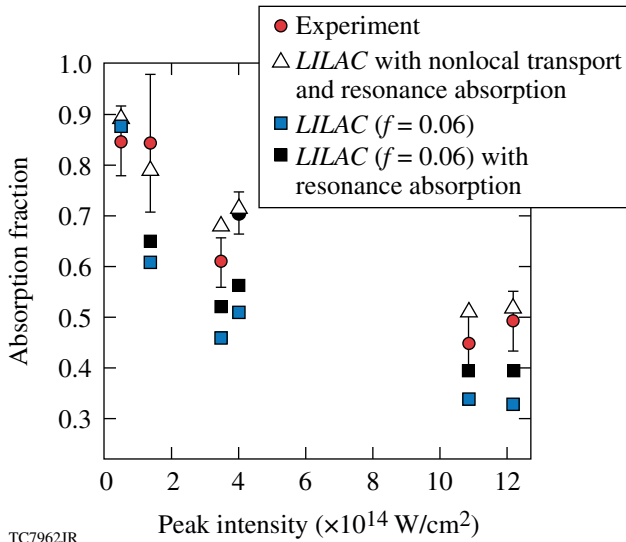
TC7962JR

Figure 130.32
Absorption fraction of the incident laser energy for a 20-μm-thick CH shell driven by a 200-ps Gaussian pulse at different peak intensities.

When the nonlocal model was used, the calculated areal densities were in closer agreement with the data compared to the results of the flux-limited model (see Fig. 130.33). Nevertheless, some discrepancies in ρR, especially for implosions with the lowest adiabat, still remained.
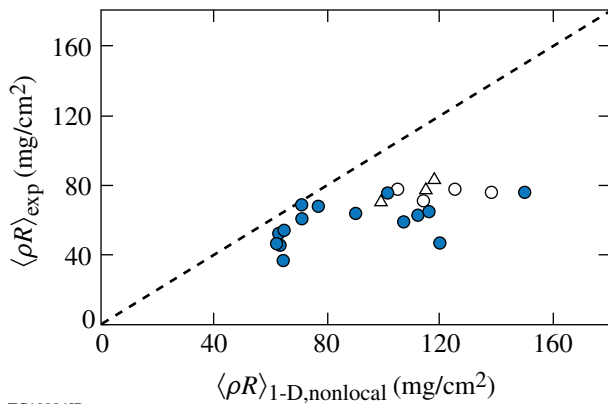
TC10004JR

Figure 130.33
Same as in Fig. 130.29, except these calculations were performed using the nonlocal thermal transport model.

The next step in the cryogenic campaign was to redesign the drive pulse design, taking into account modified coupling efficiency early in the pulse, as predicted by the new thermal transport model. Both the RX and DS designs driven at peak intensities of ~6 × 10^14 W/cm² were used in this "retuning" campaign. The experimental ρR values have marginally improved from 80 up to 100 mg/cm² (looking at this result with the knowledge that we have now, this 20% increase in areal density was mainly due to a reduction in peak intensity from 9 to 6 × 10^14 W/cm², which also reduced the strength of secondary hydrodynamic waves launched by the pulse) but fell short of predicted values that were in the range of 150 to 170 mg/cm². Even though this campaign did not succeed in significantly increasing areal densities, it revealed a very interesting trend: the measured areal densities showed very strong dependence on CD shell thickness. These results are plotted in Fig. 130.34. Such a dependence was not predicted in hydrocode simulations. Among the hypotheses explaining
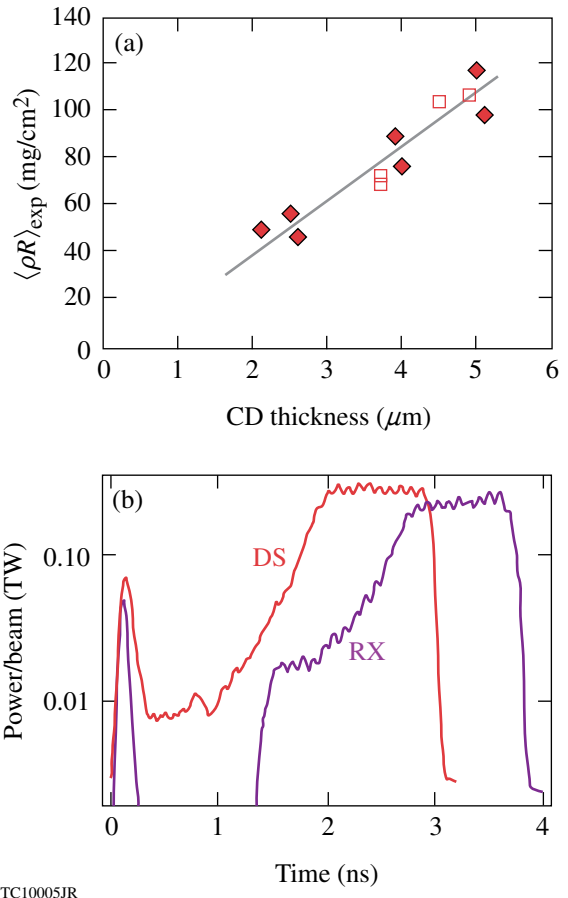
TC10005JR

Figure 130.34
(a) Measured areal densities as a function of CD shell thickness and (b) pulse shapes used in this series. DS: decaying shock; RX: relaxation.

this trend are radiation preheat caused by mix at the CD–D_2 interface (as discussed in **Radiation Preheat**, p. 91), increased preheat as a result of suprathermal electron generation by the TPD instability, or short-scale magnetic-field generation at the CH–D_2 interface as the latter travels through the ablation front and conduction zone. None of these hypotheses, however, could account for a factor-of-2.5 reduction in areal density when the CD thickness decreased from 5 to 2.5 μm. The true explanation of this observation is still not found.

b. Suprathermal electrons generated by two-plasmon-decay (TPD) instability. In parallel to the study of the effect of nonlocal thermal transport on implosion performance, a different cryogenic design was proposed and used on OMEGA experiments to address a possible preheat issue caused by the suprathermal electrons created by the TPD instability. The threshold factor for the absolute TPD instability[65] is

$$\eta = \frac{I_{14}L_n(\mu m)}{230\,T_{keV}}. \qquad (65)$$

It exceeds unity in direct-drive implosions on OMEGA when drive intensities are above $\sim 3 \times 10^{14}$ W/cm^2. Here, I_{14} is the laser intensity at quarter-critical surface in units of 10^{14} W/cm^2, L_n is the electron-density scale length in microns, and T is the electron temperature in keV. At these intensities, hard x-ray bremsstrahlung radiation, emitted by suprathermal electrons as they slow down in the plasma, is observed in OMEGA implosions[66] (see dotted line in Fig. 130.35). To prove that the preheat signal has its origin in the TPD instability, the measured hard x-ray signal must correlate with $3/2\omega$ and $\omega/2$ emission.[63] An example of such a correlation in a cryogenic implosion with a 5-μm CD shell is shown in Fig. 130.35. Here, an $\omega/2$ signal is shown with a thick green solid line. Both signals are observed when the calculated threshold parameter (shown by the dashed line marked "Threshold η") exceeds unity. The scale length for OMEGA spherical implosions, $L_n \simeq 150\ \mu$m, is set by the target size. Therefore, the main parameter that controls the TPD instability in an experiment is the laser intensity. Since the hard x-ray emission increases with laser intensity,[66] as plotted in Fig. 130.36, a "low-intensity" series of cryogenic implosions were designed with peak laser intensity reduced to below 3×10^{14} W/cm^2. Lowering drive intensity eliminates a possibility of fuel preheating caused by the suprathermal electrons.[67] The first results of this campaign, shown in Fig. 130.37(a) by three solid circles, were very encouraging: for the first time the areal density measured in a low-adiabat ($\alpha \sim 3$) cryogenic implosion agreed with the simulation result! This initial success in the
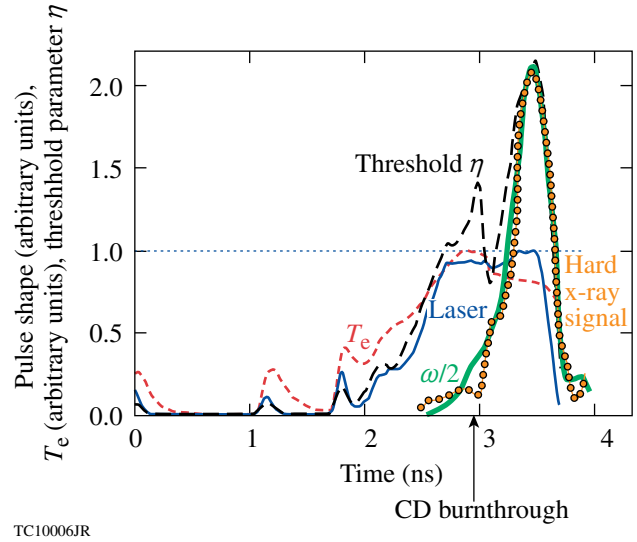

Figure 130.35
Laser pulse shape (thin solid line), electron temperature at quarter-critical surface (short-dashed line), TPD instability threshold factor (long-dashed line), measured hard x-ray signal (dotted line), and measured $\omega/2$ signal (green solid line) for a cryogenic implosion with a 5-μm-thick CD shell.

ability to accurately predict fuel compression in a cryogenic implosion, however, was short lived. With the goal of increasing areal density in a low-drive design, the first picket energy was reduced and the intensity foot was reduced and extended in time [see dashed line in Fig. 130.37(b)]. The measurements, however, showed no areal density increase predicted in simulations [see open circles in Fig. 130.37(a)]. Instead, the data followed the same trend observed in higher-intensity
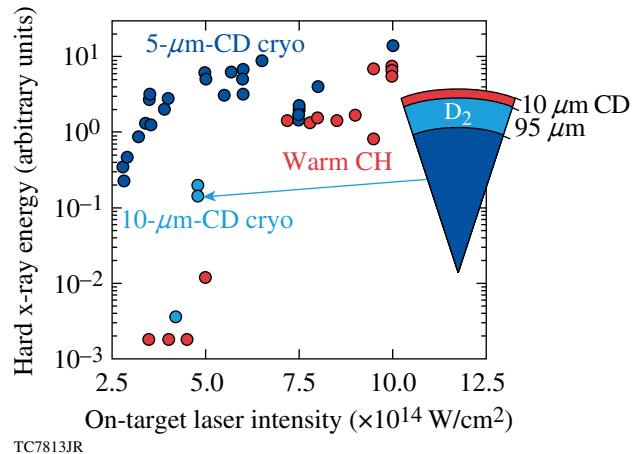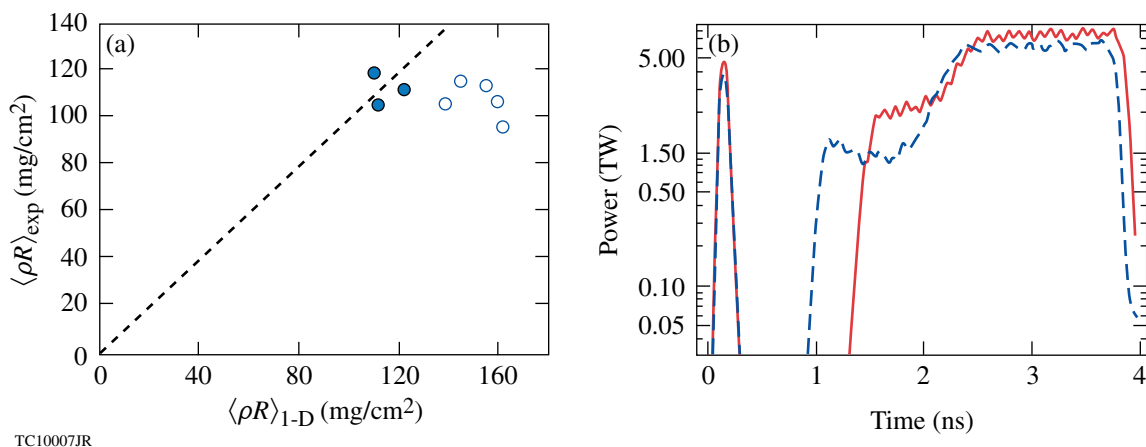

Figure 130.36
Measured energy of hard x rays (above 40 keV) as a function of incident laser intensity for a variety of OMEGA implosions.
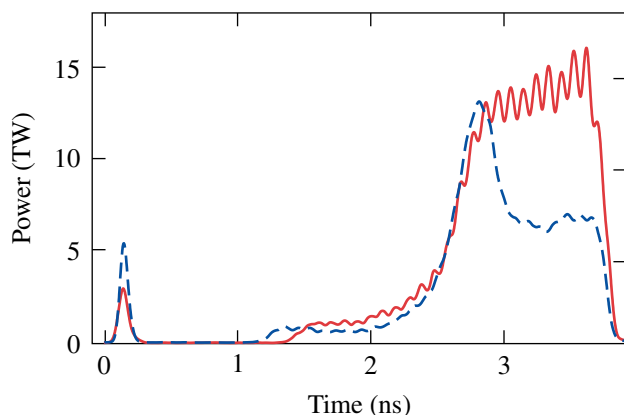
Figure 130.37

(a) Measured and (b) predicted areal densities for low-intensity RX drive pulses. Solid symbols correspond to the design shown with the solid red line in (b). The open symbols correspond to the lower-adiabat design shown with the dashed line in (b).

implosions: areal density saturated at a value independent of the predicted adiabat.

Additional evidence supporting the conclusion that the suprathermal electrons alone cannot explain the areal density degradation (as shown in Fig. 130.33) was obtained using a "dropping-intensity" design, where the drive intensity was reduced from its peak value of 5×10^{14} down to 3×10^{14} W/cm^2 starting from the time of onset of the suprathermal electron generation. This design and its comparison with the original flat-top design are shown in Fig. 130.38. While the suprathermal electron preheat signal was substantially reduced, the dropping-intensity design has also failed to achieve areal densities above the saturation value of 80 to 100 mg/cm^2.

Figure 130.38

The original (solid red line) and modified (dashed line) design to reduce suprathermal electron production.

c. Radiation preheat. In addressing the second scenario for ρR degradation, excessive radiation preheating of the main fuel, the radiation x-ray power from plasma corona was measured using Dante.[68] Figure 130.39(a) shows the total radiated x-ray power as a function of time for cryogenic implosion with a 5-μm-thick CD shell. The result of a *LILAC* simulation is also plotted. The measured radiation power starts to deviate from the predictions at 3 ns. An x-ray radiation spectrum, plotted in Figs. 130.39(b) and 130.39(c), also shows agreement with calculations early in the pulse. The spectrum deviates from calculations at $t = 3.48$ ns in the energy range from 100 eV to 1 keV. The plastic shell is totally ablated by that time, and the CD–D$_2$ interface starts to move into the plasma corona. Radiation in the hydrocode calculation diminishes at this time because a higher-Z carbon is replaced by a lower-Z hydrogen in the x-ray–emitting region. Experimental data, on the other hand, showed a persistent signal after the burnthrough time. One plausible explanation of this effect is the mix of carbon and hydrogen at the CD–D$_2$ interface. This would cause carbon to stay longer at the higher-density region and significantly enhance the radiated x-ray power. An estimated 200 J was irradiated from the plasma corona in this experiment in excess of hydrocode predictions. Based on these observations, a new target design was proposed for cryogenic implosions on OMEGA.

d. Thick plastic cryogenic designs. Observations of an enhanced x-ray emission showed that increasing the CD shell thickness from 5 to 10 μm is beneficial. The thicker shell is predicted to ablate just at the end of the pulse, protecting the fuel layer from any excessive radiation in the corona. Thicker plastic ablators also increase the threshold factor of the TPD instabil-
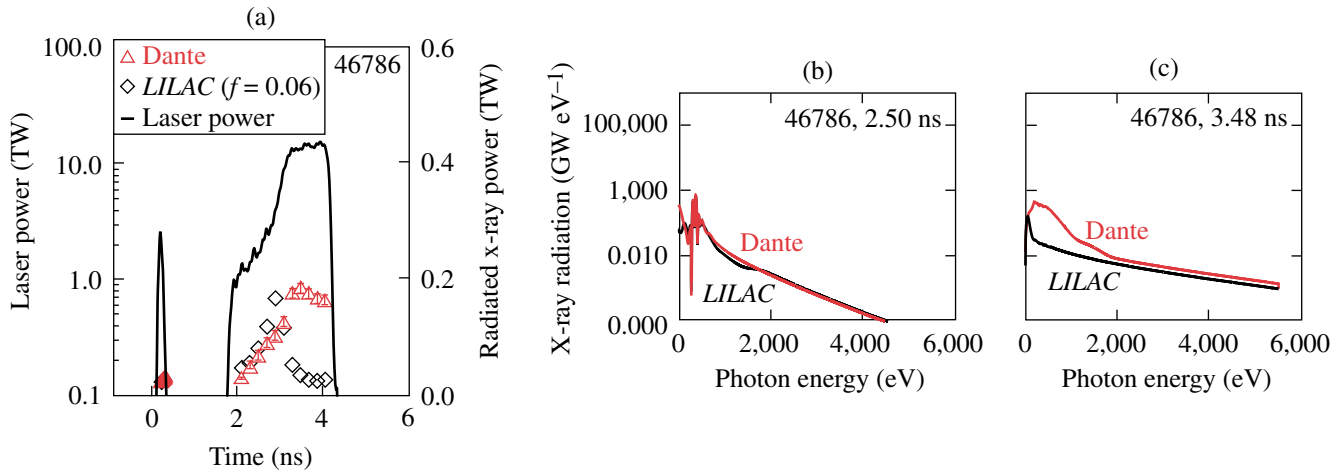
Figure 130.39

(a) Total radiated x-ray power and pulse shape and (b) x-ray radiation spectrum as measured using Dante at t = 2.5 ns and (c) t = 3.48 ns.

ity later in the pulse by raising the temperature in the plasma corona. Such a temperature increase is caused by a larger laser absorption fraction caused by the presence of higher-Z carbon in the absorption region. A higher absorption fraction farther away in the corona also reduces irradiation intensity that reaches a quarter-critical surface. Both these effects lead to a reduction in η [see Eq. (65)]. The cryogenic design with a 10-μm-thick CD ablator driven at $\sim 5 \times 10^{14}$ W/cm^2 is shown in Fig. 130.40. Four shots with this design produced areal densities 200 mg/cm^2, matching code predictions.[57,69] Figure 130.41 shows predicted
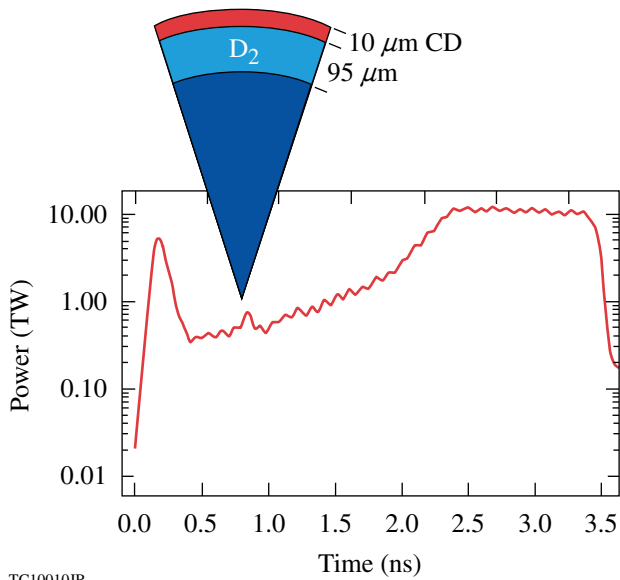

Figure 130.40

Pulse shape and target dimensions for the thick plastic cryogenic design.

and measured spectra of down-scattered secondary protons, confirming prediction accuracy. The areal densities and fuel compression in these implosions were the highest ever achieved in an ICF implosion. As expected, both the hard x-ray signal (see points marked "10-μm-CD cryo" in Fig. 130.36) and x-ray energy below 1 keV, emitted in excess to the predicted value, were significantly reduced in these experiments.

Even though the designs with a thicker ablator demonstrated high compression, the drive intensity and implosion velocity $V_{imp} \sim 2.2 \times 10^7$ cm/s were smaller than required for a robust direct-drive–ignition design, $I \sim 8 \times 10^{14}$ W/cm^2 and $V_{imp} > 3.5 \times 10^7$ cm/s, respectively (see **A Simple Ignition Model**, p. 72). The next step was to increase both the drive intensity and the implosion velocity (by reducing the shell mass). This turned out to be a very challenging task. Figure 130.42(a) shows modifications made to the pulse shape in an attempt to increase the drive intensity. Raising the intensity also increases the electron preheat signal. Figure 130.42(b) shows measured areal densities as a function of the preheat signal (solid symbols). The measured areal density decreased dramatically even for minor variations in the laser pulse with very little or no sensitivity to the preheat signal. Reducing the thickness of the frozen D$_2$ layer from 95 to 80 μm also resulted in a decreased measured areal density (the predictions were ~ 200 mg/cm^2 for all cases). This is shown with open symbols in Fig. 130.42(b) . These results demonstrated that the continuous-pulse designs cannot be easily extended to the ignition-relevant drive intensities and implosion velocities.

e. Shock heating. The breakthrough in understanding cryogenic target performance came in 2008 when the shock-velocity

measurement technique matured enough to give information on the formation of shock and compression waves in spherical geometry.[70] These measurements addressed the third scenario for explaining areal-density degradation—excessive shock heating. Accuracy of shock timing was verified by measuring the velocity of the 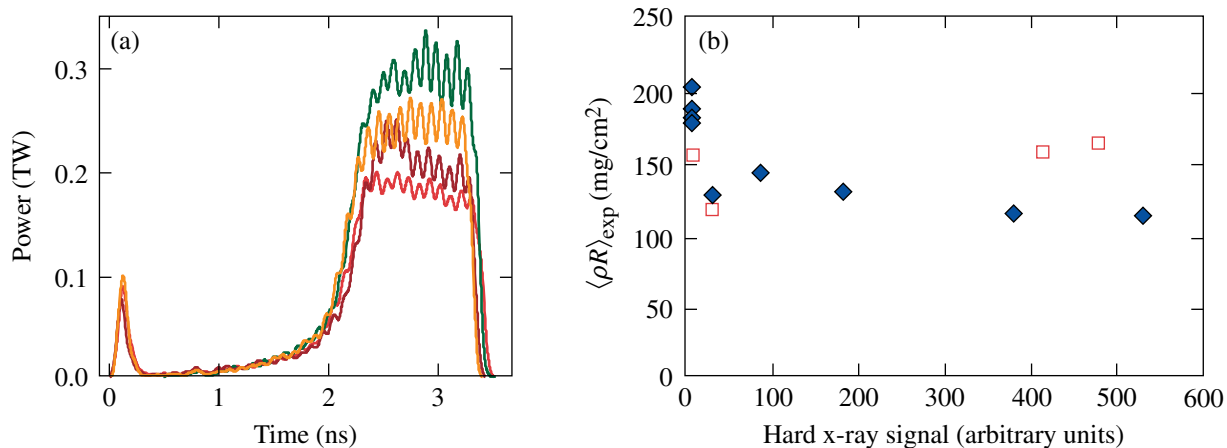leading shock wave using the velocity interferometry system for any reflector (VISAR).[71] The targets in these experiments were spherical, 5- or 10-μm-thick CD shells fitted with a diagnostic cone. The shell and cone were filled with liquid deuterium. An example of VISAR measurement performed using the continuous pulse design is shown in Fig. 130.43. The measured shock velocity, as a function of
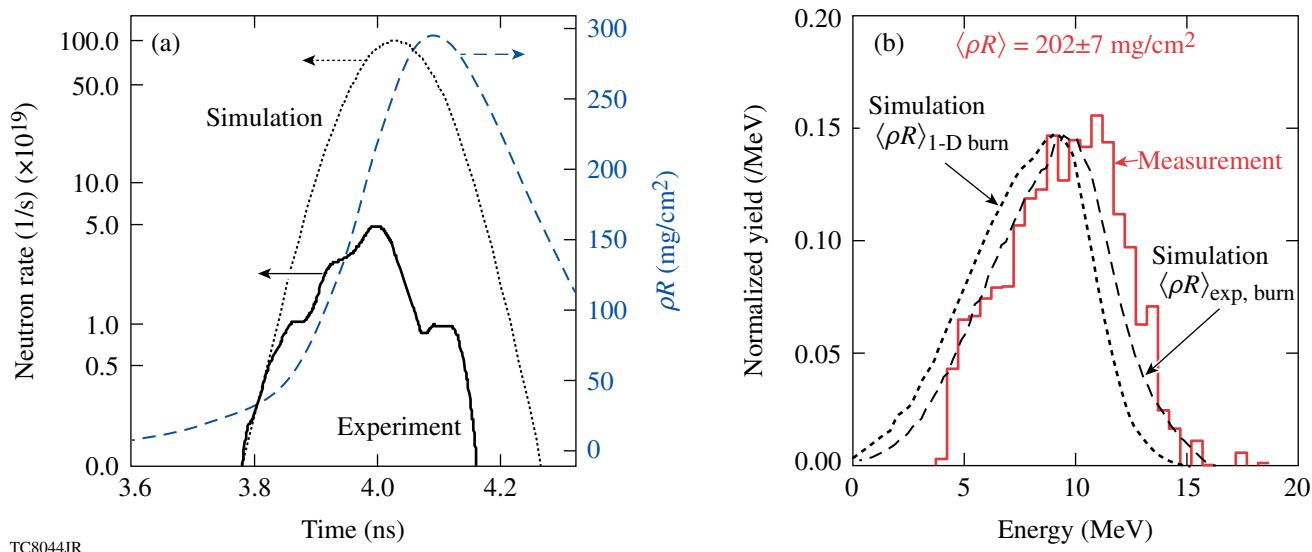
Figure 130.41

(a) The neutron-production history measured (solid line) and predicted (dotted line) for the design shown in Fig. 130.40. The ρR evolution calculated using the 1-D code *LILAC* (dashed line, right axis) is also shown. (b) Measured secondary-proton spectrum (solid line). The dotted line shows the calculated spectrum averaged over the predicted 1-D neutron production, and the dashed line represents the calculated spectrum averaged over the experimental neutron-production history.

Figure 130.42

(a) Variation to the target design shown in Fig. 130.40 and (b) resulting measured areal densities for designs with 95-μm (solid symbols) and 80-μm (open symbols) D$_2$ ice thickness.
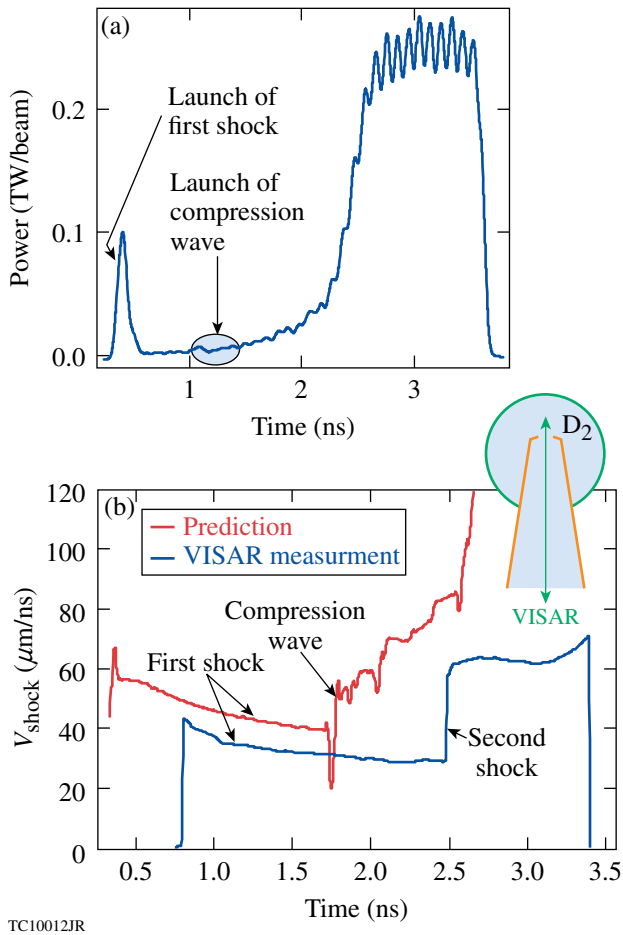
Figure 130.43

(a) Pulse shape and (b) leading shock velocity measured (lower curve) and predicted (upper curve).

Figure 130.44

Two- (dashed line) and three-picket (solid line) cryogenic OMEGA target designs.

After obtaining the VISAR results, the cryogenic program at LLE quickly moved to multiple-picket designs[72] by introducing double-picket and, later, triple-picket pulses (see Fig. 130.44). To set the fuel on a low adiabat $\alpha \sim 1$ to 3, the double-picket design still requires a moderate-intensity foot (1/4 to 1/3 of peak intensity) and a gradual intensity increase to compress the fuel adiabatically (dashed line in Fig. 130.44). The triple-picket design (solid line in Fig. 130.44), on the other hand, does not rely on an adiabatic compression and requires a short step at the beginning of the main pulse to control the strength of the main shock.
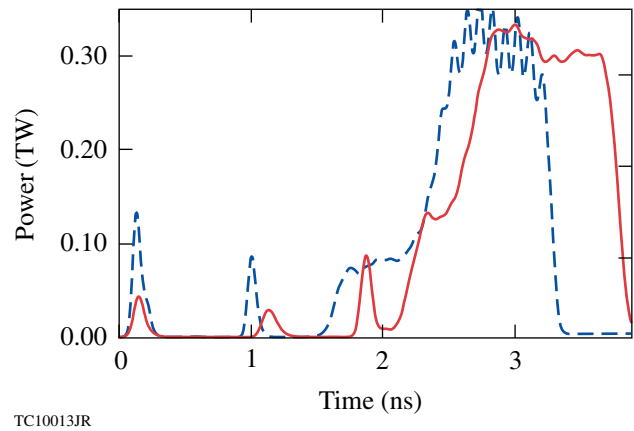
**Current Triple-Picket Cryogenic-DT Implosions**

The main advantage in using multiple-picket designs is the ability to control all hydrodynamic waves launched by the drive pulse.[72] As described in **All-DT, Direct-Drive, NIF-Scale Ignition Target Design** (p. 76), designs with continuous pulses rely on adiabatic fuel compression while the drive pressure increases by a factor of 50 or more. The observed premature steepening of the adiabatic compression wave into a shock inside the shell makes it impractical to experimentally tune the shell adiabat in these designs. In the multiple-picket designs shown in Fig. 130.44, the required increase in drive pressure from a few Mbar to ~100 Mbar is accomplished by launching a sequence of shocks that can be well controlled by adjusting the timing and energy of each individual intensity picket. Two types of the triple-picket pulse shapes are used in current cryogenic implosions on OMEGA. The laser power in the first design, shown in Fig. 130.45(a), consists of three pickets and the main drive in the form of a square pulse. To control the strength of the main shock, a short intensity step is introduced at the beginning of the main drive in the second design [shown

time, is compared with 1-D predictions obtained using a *LILAC* simulation. An intensity picket at the beginning of the drive pulse sends a shock wave of decaying strength. As the drive intensity starts to rise from its minimum value, a compression wave is launched into the ablator at $t \simeq 1$ ns. After the head of the compression catches up with the first shock, strength and velocity of the leading shock increase gradually in time. The measured velocity history, however, shows a much steeper velocity increase that takes place later in the pulse, indicating that the compression wave turns into a shock prior to its coalescence with the first shock. Such a transition from adiabatic to shock compression raises the fuel adiabat at the inner part of the shell, limiting the final target convergence and peak fuel ρR. Since the effect of the compression wave steepening into a shock, not predicted by a simulation, is exacerbated by an increasing peak drive pulse or changing the shell thickness, difficulty in tuning continuous-pulse designs can be explained by excessive shock heating.

in Fig. 130.45(b)]. The stronger main shock launched in the first design sets the fuel on $\alpha = 2.5$ to 3. A weaker shock in the second design reduces the adiabat to $\alpha = 2$ to 2.5. Next, we describe how shock tuning was accomplished in these designs using OMEGA experiments.

1. Shock Tuning

Accuracy in predicting shock timing is verified by measuring the velocity of the leading shock wave using VISAR. The targets in these experiments were spherical, 5- or 10-μm-thick CD shells fitted with a diagnostic cone.[73] The shell and cone were filled with liquid deuterium. For an optimized design,[72]

all shocks should coalesce within 100 ps, soon after they break out of the shell. For the purpose of code validation, the time separation between shock coalescence events was increased in these experiments to accurately infer leading shock velocity after each coalescence. An example of such a measurement is shown in Fig. 130.46. Because of radiation precursor, the shock is not visible to VISAR early in time while it travels through the plastic layer. Then, at $t \sim 300$ ps, the shock breaks out of CD into D_2 with a velocity of ~ 60 μm/ns. The shock is not supported by the laser at this time (picket duration is ~ 80 ps). Therefore, the shock strength and its velocity decrease with time. Then, the second shock is launched at $t = 1.1$ ns. It travels through
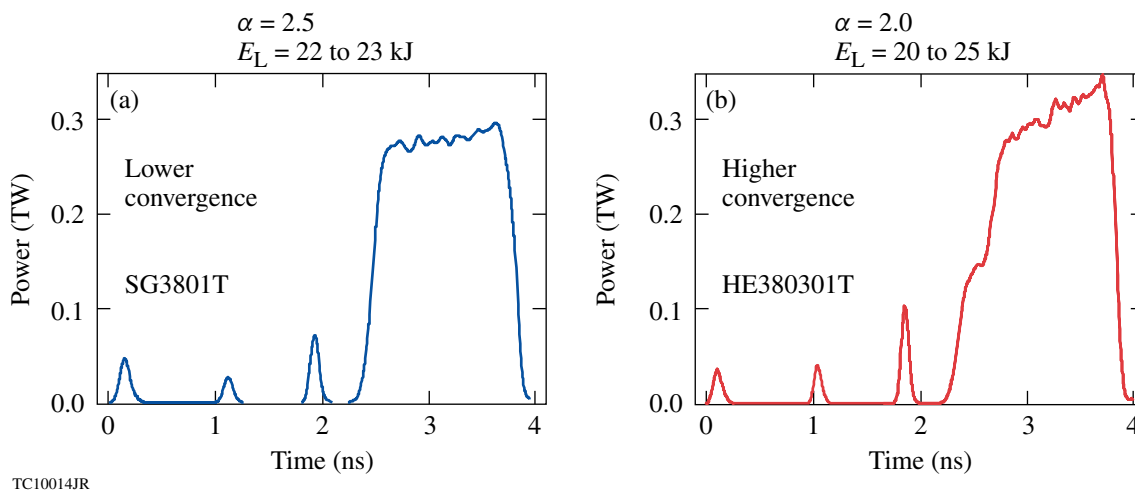
Figure 130.45
Two triple-picket target designs used in cryogenic implosions on OMEGA.
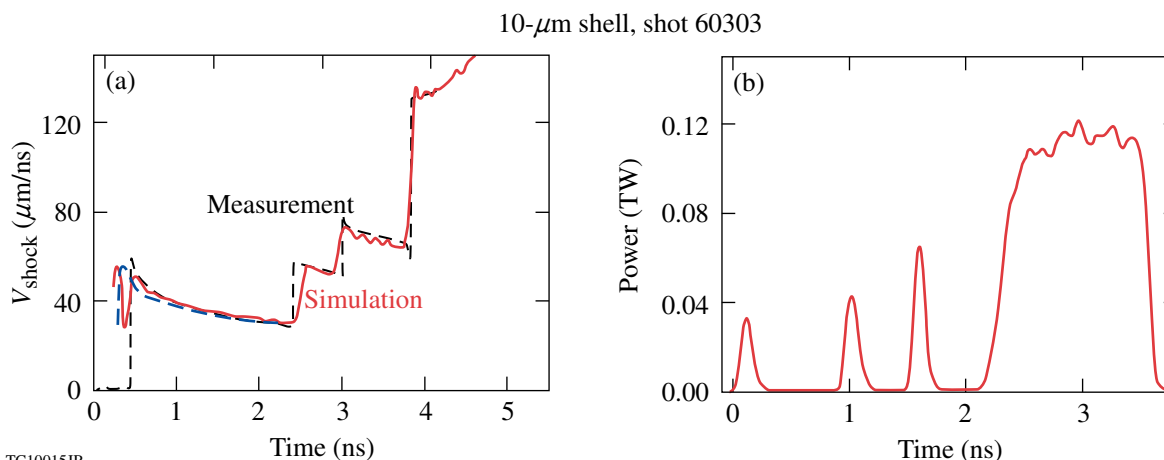
Figure 130.46
(a) Measured (dashed line) and predicted (solid line) leading shock velocity in (b) a triple-picket design.

the relaxed density and pressure profiles established by the first shock. At $t = 2.5$ ns the second shock catches up with the first, resulting in a jump in leading shock velocity from 35 up to 60 μm/ns. The third picket and the main pulse launch two additional shocks that coalesce with the leading shock at $t = 3.0$ and 3.9 ns, respectively.

Matching both shock velocities and coalescence times is a good test of a thermal-conduction model used in a hydrocode simulation. The thermal conduction affects hydrodynamic profiles that determine energy coupling. The flux-limited model with $f = 0.06$ predicts a lower laser-absorption fraction than that calculated using the nonlocal thermal transport model, leading to a slower shock. The difference between two transport models increases with the energy in the first picket. The comparison between model predictions and experimental data is shown in Fig. 130.47. As seen in this figure, agreement between prediction and measurement improves when the nonlocal thermal-transport model is used in the simulations.
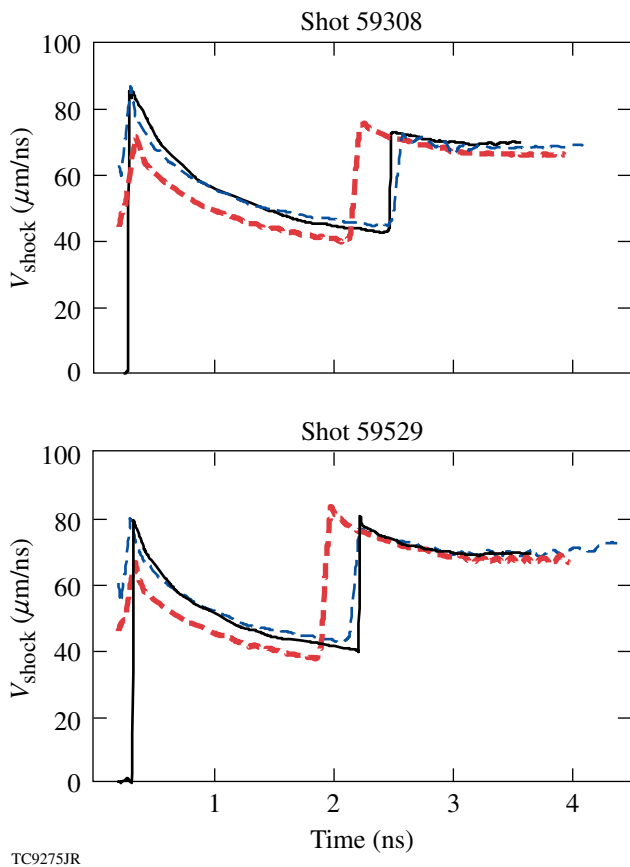

Figure 130.47
Measured (solid lines) and predicted leading shock velocity using the flux-limited (thick red dashed lines) and nonlocal (thin dashed lines) electron thermal-transport models for two shots.

Matching the predicted and measured shock velocities and coalescence times ensures that the shock heating is properly modeled. The in-flight shell adiabat, set by the shocks, can be degraded during the implosion by electron or radiation preheat as well as by secondary shock waves. As described in **Adiabat** (p. 81), the in-flight adiabat can be inferred from areal-density measurements if no significant shell decompression is induced by the prolonged coasting phase [see discussion after Eq. (53)]. The extended coasting phase could result from a loss in hydro-efficiency during shell acceleration. The latter would reduce shell implosion velocity and delay the time of neutron production. Therefore, to connect any observable degradation in areal density with fuel preheat or any other effects that enhance in-flight adiabat, one must verify that hydrodynamic efficiency is accurately modeled and no extended coasting phase is present in the implosion. This will be addressed in the next subsection.

2. Laser Coupling and Hydrodynamic Efficiency
Accurate modeling of hydrodynamic efficiency of an imploding shell (defined as the ratio of the peak in shell kinetic energy to the total laser energy) is crucial for optimizing high-convergence target designs, since a loss in the shell's implosion velocity and kinetic energy leads to shell coasting after the laser drive turns off. During such coasting, both shell density and pressure drop. This reduces ρR [see Eq. (53)] and gives a lower fuel ion temperature at the time of neutron production. One of the diagnostics that is most sensitive to deviations in the shell's implosion velocity is a measurement of timing and temporal shape of primary neutrons produced as a result of fusion reactions. This is accomplished by using NTD (see discussion in **Implosion Velocity**, p. 84). Currently, NTD is calibrated on OMEGA to ~50-ps absolute timing accuracy with ~10-ps shot-to-shot timing variation. In addition to the neutron-production timing, the laser-absorption measurement is performed using two full-aperture backscattering stations (FABS).[63] Time-resolved scattered-light spectroscopy and time-integrated calorimetry in these stations are used to infer the absorption of laser light. Laser absorption, however, is not a direct measurement of hydrodynamic efficiency since only a small fraction of the incident laser energy (~5%) is converted (through the mass ablation) into the shell's kinetic energy and the majority of the absorbed energy goes into heating the under-dense plasma corona. Also, some fraction of laser energy can be deposited into plasma waves that accelerate suprathermal electrons and do not directly contribute to the drive.

Figures 130.48(a) and 130.48(b) compare the measured scattered laser light and Fig. 130.48(c) compares neutron pro-duction history with the predictions (blue solid lines represent
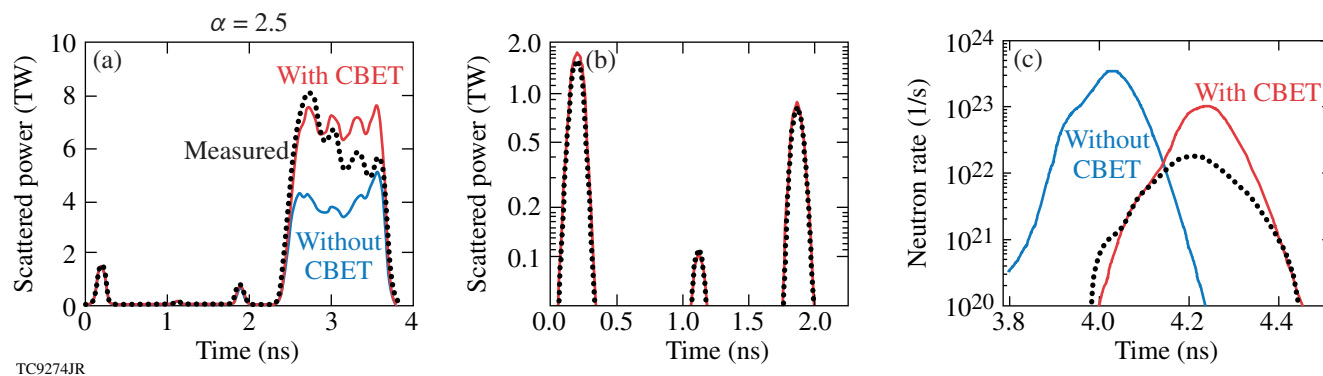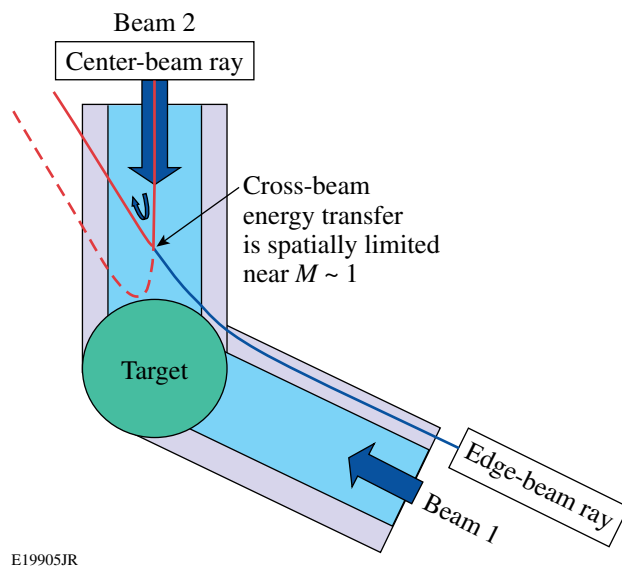
Figure 130.48

[(a) and (b)] Measured (dotted lines) and predicted (solid lines) scattered-light data. (c) Neutron-production history for the $\alpha = 2.5$ design shown in Fig. 130.45(a).

without CBET) for an $\alpha = 2.5$ design. As seen in Fig. 130.48(b), calculations are in very good agreement with the measured scattered-light data (dotted line) for the picket portion of the pulse. At the main drive, however, the predicted laser absorption overestimates the data, especially at the beginning of the drive. Higher predicted laser coupling results in an earlier bang time, as shown in Fig. 130.48(c). On average, the rise of the neutron rate is earlier in simulations by 200 ps. Since calculations fail to accurately reproduce the laser-absorption fraction and neutron-production timing, an additional mechanism explaining a reduced laser coupling must be present in the experiments.

Such a mechanism, as discussed in a recent publication,[74] is due to the cross-beam energy transfer (CBET).[75] In the geometric optics approximation where each laser beam is subdivided into rays, the incoming ray in the central part of the beam interacts (through the ion-acoustic waves) with the outgoing ray on the outer edge of the beam, transferring its energy to that ray. This is illustrated in Fig. 130.49. Since the central part of the beam propagates closest to the target, CBET reduces the fraction of the beam energy that reaches the higher-density plasma corona, decreasing overall laser absorption. Because CBET reduces the total laser absorption, and, furthermore, the absorbed energy is deposited in corona farther away from the target surface, the hydroefficiency of laser drive in directly driven implosions is degraded by 15% to 20% in OMEGA implosions. When implemented into the hydrocode *LILAC*, a CBET model predicts a 10% to 15% reduction in the absorbed energy, in agreement with experimental data. Shown in Fig. 130.48 solid lines marked "with CBET" are (a) the scattered light and (c) neutron-production rate calculated using a combination of the nonlocal thermal transport and CBET models. The neutron-production timing matches data very well. The scattered-light power, however, deviates from the measurements at later times. This late-time discrepancy is likely due

Figure 130.49

The incoming ray in the central part of Beam 2 interacts with the outgoing ray on the outer edge of Beam 1, transferring its energy to that ray.

to extra absorption of laser energy by plasma waves excited by the TPD instability.[14] Figure 130.50 shows the drive pulses and threshold parameters for $\alpha = 2.5$ designs. The threshold parameter first oscillates around $\eta = 1$ and then rises above unity at $t \sim 3.2$ to 3.3 ns. This matches the time when the experimental scattered light starts deviating from the predictions. To further support the assertion that the observable fraction of laser energy is being deposited into plasma waves, the scattered-light measurement and prediction are plotted in Fig. 130.51 for an implosion at a slightly higher drive intensity where the TPD instability threshold is exceeded at the beginning of the main drive [see Fig. 130.51(b)]. The calculated scattered-light power starts deviating from measurements earlier in this case, which is consistent with the timing of η exceeding unity.

Incorporating the CBET model into hydrocode simulations shows only a marginal reduction (on average by ~5%) in neutron-averaged areal densities. This confirms that the areal

TC9283JR

Figure 130.50
Pulse shape (dashed line) and threshold parameter η of TPD instability.

TC9285JR

Figure 130.51
(a) Measured (dotted line) and predicted scattered power. (b) Pulse shape (dashed line) and threshold parameter η of TPD instability (solid line).

densities in cryogenic implosions on OMEGA are affected mainly by the in-flight shell adiabat and the effect of shell decompression during the coasting phase is small.

3. Areal Densities in a Triple-Picket Cryogenic Implosions

In this section we compare the calculated neutron-averaged areal density $\langle \rho R \rangle_n$ with the measurements. Since the predicted $\langle \rho R \rangle_n \sim 150$ to 200 mg/cm^2 for $\alpha = 2.5$ and $\langle \rho R \rangle_n \sim 220$ to 300 mg/cm^2 for $\alpha = 2$, the areal density is currently inferred using a single-view measurement with a magnetic recoil spectrometer (MRS).[28] The MRS measures the number of primary neutrons and the number of neutrons scattered in the dense DT fuel. The ratio of these two is proportional to the fuel areal density during the neutron production. Two charged-particle spectrometers (CPS's) were also used to measure the spectrum of knock-on deuterons, elastically scattered by primary DT neutrons. These measurements, however, are insensitive to $\langle \rho R \rangle_n > 180$ mg/cm^2 and were used to assess low-ℓ-mode ρR asymmetries for implosions where areal density along the CPS's line of sight is below 180 mg/cm^2. Such asymmetries arise from errors in target positioning (offset) and ice roughness amplified during shell implosion. Since only a single-view MRS measurement is used for ρR analysis, it is important to take long-wavelength asymmetries into account when comparing the simulated and measured areal densities for high-convergence implosions. Strictly speaking, even a single MRS measurement averages fuel ρR over a solid angle of ~1.5π since the down-scattered neutrons have a finite spectral width and neutrons with different energies sample different parts of the shell (see Fig. 130.52). The scattering angle θ of a primary neutron (marked with "n" in Fig. 130.52) depends on down-scattered neutron ("n'") energy. MRS is sensitive to 8- to 13-MeV neutrons. The minimum scattering angle $\theta_{min} = 29°$ and $23°$ correspond to 13-MeV neutrons scattered by tritons and deuterons, respectively. The maximum angle $\theta_{max} = 80°$ and $62°$ corresponds to 8-MeV neutrons. The dark shell region in Fig. 130.52 corresponds to a region sampled by the down-scattered neutrons in a single-view MRS measurement on OMEGA. Taking into account such averaging, Fig. 130.53 plots a calculated variation in areal density as would be observed by the MRS in a single-view measurement taken along a different direction with respect to the target offset. The results are shown for the offset values of $\Delta_{offset} = 10$ μm (black line) and 30 μm (green line). The calculations were performed by post-processing results of 2-D *DRACO* simulations[76] using the Monte Carlo–based particle transport code *IRIS*. The error bars in Fig. 130.53 represent counting statistics errors in a typical cryogenic implosion on OMEGA. These calculations show that the $\langle \rho R \rangle_n$ variation across the target can be approximated by a linear function of the offset,
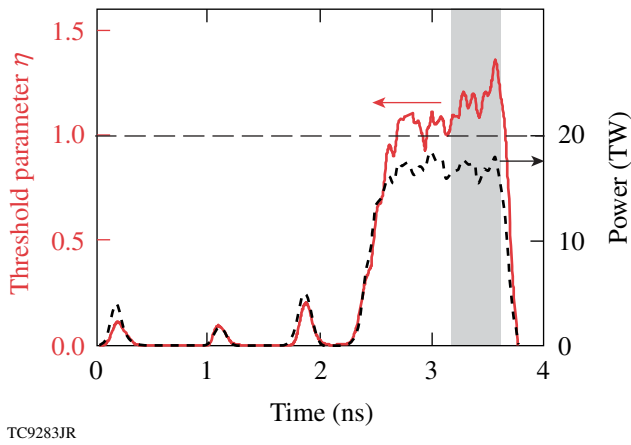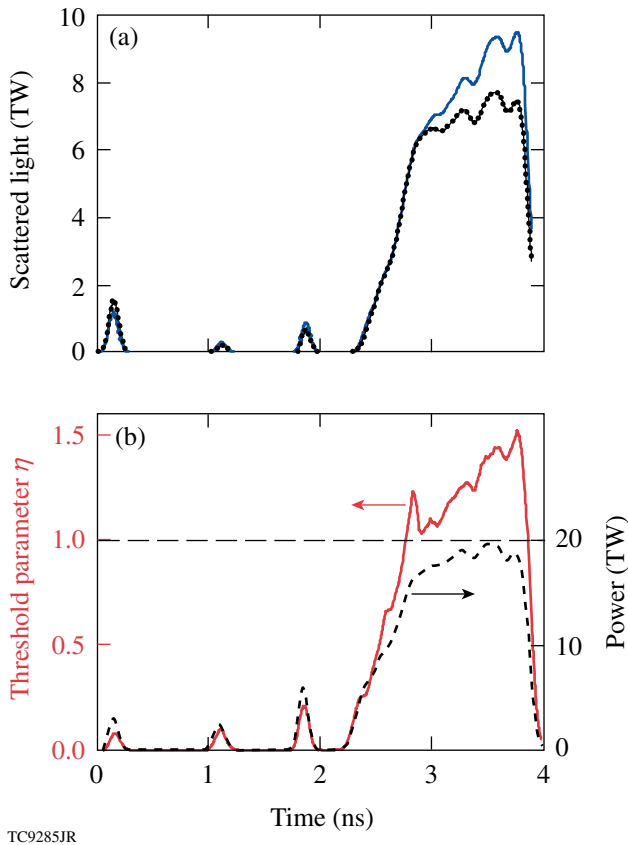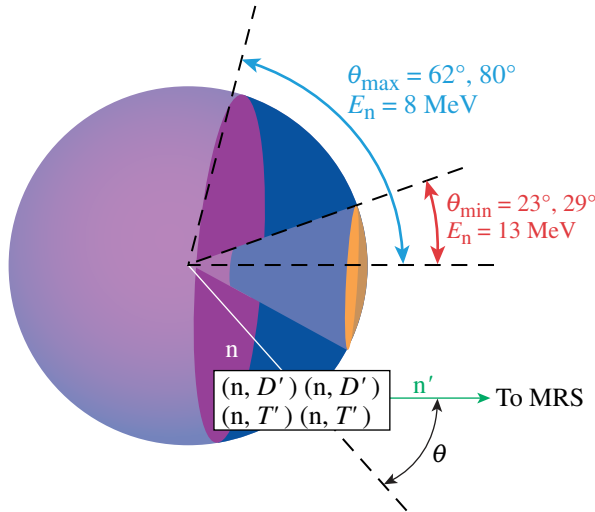
$$\frac{\max\langle\rho R\rangle_{n} - \min\langle\rho R\rangle_{n}}{\langle\rho R\rangle_{n}}\% \simeq \Delta_{\text{offset}}\left(\mu m\right). \qquad (66)$$

In addition to the target offset, the low-ℓ modes ($\ell \leq 2$) seeded by the ice roughness also lead to an azimuthal variation in the


TC9288JR

Figure 130.52

The scattering angle θ of a primary neutron (marked with "n") depends on down-scattered neutron ("n'") energy. MRS is sensitive to neutrons with energies between 8 and 13 MeV. The minimum scattering angles $\theta_{\min} = 29°$ and 23° correspond to 13-MeV neutrons scattered by tritons and deuterons, respectively. The maximum angles $\theta_{\max} = 80°$ and 62° correspond to 8-MeV neutrons. The dark shell region corresponds to a region sampled by the down-scattered neutrons in a single-view MRS measurement on OMEGA.

measured areal density. In plotting the predicted $\langle\rho R\rangle_{n}$, we assign the error bar for each point taking into account the ρR variation caused by target offset and low-mode ice roughness measured for each target. The result is shown in Fig. 130.54 (see also Ref. 72), where squares and circles correspond to $\alpha = 2$ and $\alpha = 2.5$ designs, respectively. In general, there is good agreement between the experimental data and calculations. This confirms that the adiabat is modeled accurately in low-adiabat cryogenic implosions on OMEGA using the triple-picket designs.
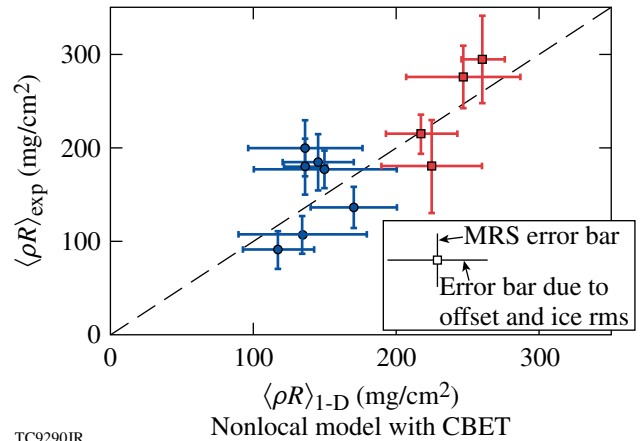

TC9290JR

Figure 130.54

Measured versus predicted areal densities for triple-picket cryogenic implosions on OMEGA.
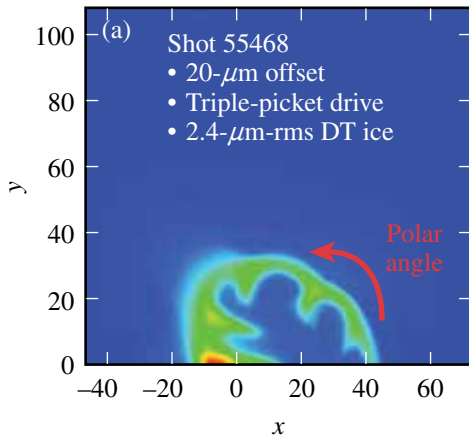
TC9289JR

Figure 130.53

(a) Density contour of 2-D *DRACO* simulation of a cryogenic implosion on OMEGA (shot 55468) with a target offset of 20 μm. (b) Predicted variation in areal density as would be observed by the MRS in a single-view measurement taken along a different direction with respect to the target offset.
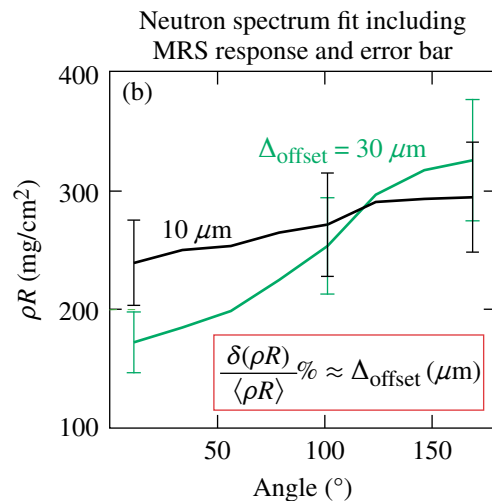
Based on the good performance of the triple-picket design on OMEGA, this design was extended to a 1.5-MJ direct-drive–ignition design[72] for the National Ignition Facility (see Fig. 130.55). Driven at a peak intensity of 8×10^{14} W/cm^2, the shell reaches $V_{\text{imp}} = 3.5$ to 4×10^7 cm/s, depending on the thickness of the fuel layer. This design is predicted to ignite with a gain $G = 48$.
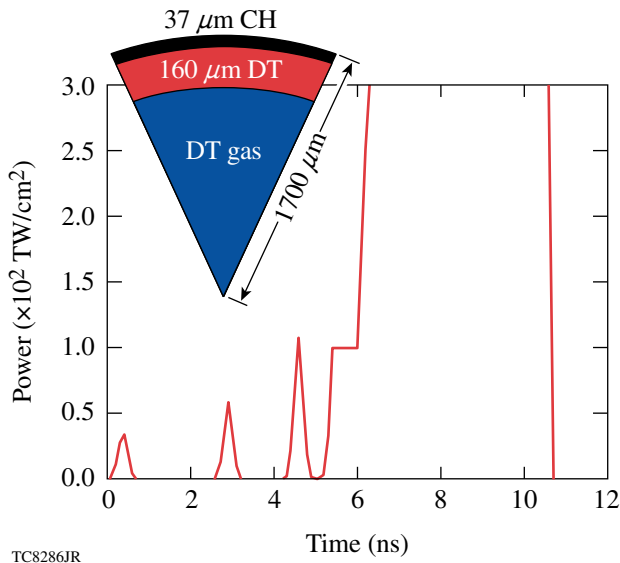

Figure 130.55
Triple-picket, symmetric direct-drive design for the NIF.

ACKNOWLEDGEMENT

REFERENCES

1. J. D. Lindl, *Inertial Confinement Fusion: The Quest for Ignition and Energy Gain Using Indirect Drive* (Springer-Verlag, New York, 1998).

2. S. Atzeni and J. Meyer-ter-Vehn, *The Physics of Inertial Fusion: Beam Plasma Interaction, Hydrodynamics, Hot Dense Matter*, International Series of Monographs on Physics (Clarendon Press, Oxford, 2004).

3. M. C. Herrmann, M. Tabak, and J. D. Lindl, Phys. Plasmas **8**, 2296 (2001).

4. R. Betti, K. Anderson, V. N. Goncharov, R. L. McCrory, D. D. Meyerhofer, S. Skupsky, and R. P. J. Town, Phys. Plasmas **9**, 2277 (2002).

5. V. N. Goncharov, in *Laser-Plasma Interactions*, edited by D. A. Jaroszynski, R. Bingham, and R. A. Cairns, Scottish Graduate Series (CRC Press, Boca Raton, FL, 2009), pp. 409–418.

6. J. Meyer-ter-Vehn, Nucl. Fusion **22**, 561 (1982).

7. R. Betti, P. Y. Chang, B. K. Spears, K. S. Anderson, J. Edwards, M. Fatenejad, J. D. Lindl, R. L. McCrory, R. Nora, and D. Shvarts, Phys. Plasmas **17**, 058102 (2010).

8. A. Kemp, J. Meyer-ter-Vehn, and S. Atzeni, Phys. Rev. Lett. **86**, 3336 (2001).

9. S. W. Haan, J. D. Lindl, D. A. Callahan, D. S. Clark, J. D. Salmonson, B. A. Hammel, L. J. Atherton, R. C. Cook, M. J. Edwards, S. Glenzer, A. V. Hamza, S. P. Hatchett, M. C. Herrmann, D. E. Hinkel, D. D. Ho, H. Huang, O. S. Jones, J. Kline, G. Kyrala, O. L. Landen, B. J. MacGowan, M. M. Marinak, D. D. Meyerhofer, J. L. Milovich, K. A. Moreno, E. I. Moses, D. H. Munro, A. Nikroo, R. E. Olson, K. Peterson, S. M. Pollaine, J. E. Ralph, H. F. Robey, B. K. Spears, P. T. Springer, L. J. Suter, C. A. Thomas, R. P. Town, R. Vesey, S. V. Weber, H. L. Wilkens, and D. C Wilson, Phys. Plasmas **18**, 051001 (2011).

10. C. P. Verdon, Bull. Am. Phys. Soc. **38**, 2010 (1993).

11. P. W. McKenty, V. N. Goncharov, R. P. J. Town, S. Skupsky, R. Betti, and R. L. McCrory, Phys. Plasmas **8**, 2315 (2001).

12. J. Paisner *et al.*, Laser Focus World **30**, 75 (1994).

13. V. N. Goncharov, S. Skupsky, T. R. Boehly, J. P. Knauer, P. McKenty, V. A. Smalyuk, R. P. J. Town, O. V. Gotchev, R. Betti, and D. D. Meyerhofer, Phys. Plasmas **7**, 2062 (2000).

14. W. L. Kruer, *The Physics of Laser–Plasma Interactions*, Frontiers in Physics, Vol. 73, edited by D. Pines (Addison-Wesley, Redwood City, CA, 1988), Chap. 4, p. 81.

15. S. Chandrasekhar, in *Hydrodynamic and Hydromagnetic Stability*, International Series of Monographs on Physics (Clarendon Press, Oxford, 1961), p. 428.

16. J. Sanz, Phys. Rev. Lett. **73**, 2700 (1994); V. N. Goncharov, R. Betti, R. L. McCrory, P. Sorotokin, and C. P. Verdon, Phys. Plasmas **3**, 1402 (1996).

17. R. Betti, V. N. Goncharov, R. L. McCrory, and C. P. Verdon, Phys. Plasmas **5**, 1446 (1998).

18. J. Sanz, Phys. Rev. E **53**, 4026 (1996).

19. V. N. Goncharov, O. V. Gotchev, E. Vianello, T. R. Boehly, J. P. Knauer, P. W. McKenty, P. B. Radha, S. P. Regan, T. C. Sangster, S. Skupsky, V. A. Smalyuk, R. Betti, R. L. McCrory, D. D. Meyerhofer, and C. Cherfils-Clérouin, Phys. Plasmas **13**, 012702 (2006).

20. V. N. Goncharov, J. P. Knauer, P. W. McKenty, P. B. Radha, T. C. Sangster, S. Skupsky, R. Betti, R. L. McCrory, and D. D. Meyerhofer, Phys. Plasmas **10**, 1906 (2003).

21. H. Sawada, S. P. Regan, D. D. Meyerhofer, I. V. Igumenshchev, V. N. Goncharov, T. R. Boehly, R. Epstein, T. C. Sangster, V. A. Smalyuk, B. Yaakobi, G. Gregori, S. H. Glenzer, and O. L. Landen, Phys. Plasmas **14**, 122703 (2007).

22. D. Zhou and R. Betti, Phys. Plasmas **14**, 072703 (2007).

23. A. L. Kritcher *et al.*, Phys. Rev. Lett. **107**, 015002 (2011).

24. H. Sawada, S. P. Regan, P. B. Radha, R. Epstein, D. Li, V. N. Goncharov, S. X. Hu, D. D. Meyerhofer, J. A. Delettrez, P. A. Jaanimagi, V. A. Smalyuk, T. R. Boehly, T. C. Sangster, B. Yaakobi, and R. C. Mancini, Phys. Plasmas **16**, 052702 (2009).

25. F. J. Marshall, P. W. McKenty, J. A. Delettrez, R. Epstein, J. P. Knauer, V. A. Smalyuk, J. A. Frenje, C. K. Li, R. D. Petrasso, F. H. Séguin, and R. C. Mancini, Phys. Rev. Lett. **102**, 185004 (2009).

26. R. Tommasini, S. P. Hatchett, D. S. Hey, C. Iglesias, N. Izumi, J. A. Koch, O. L. Landen, A. J. MacKinnon, C. Sorce, J. A. Delettrez, V. Yu. Glebov, T. C. Sangster, and C. Stoeckl, Phys. Plasmas **18**, 056309 (2011).

27. F. H. Séguin, C. K. Li, J. A. Frenje, D. G. Hicks, K. M. Green, S. Kurebayashi, R. D. Petrasso, J. M. Soures, D. D. Meyerhofer, V. Yu. Glebov, P. B. Radha, C. Stoeckl, S. Roberts, C. Sorce, T. C. Sangster, M. D. Cable, K. Fletcher, and S. Padalino, Phys. Plasmas **9**, 2725 (2002).

28. J. A. Frenje, C. K. Li, F. H. Séguin, D. T. Casey, R. D. Petrasso, T. C. Sangster, R. Betti, V. Yu. Glebov, and D. D. Meyerhofer, Phys. Plasmas **16**, 042704 (2009); J. A. Frenje, D. T. Casey, C. K. Li, F. H. Séguin, R. D. Petrasso, V. Yu. Glebov, P. B. Radha, T. C. Sangster, D. D. Meyerhofer, S. P. Hatchett, S. W. Haan, C. J. Cerjan, O. L. Landen, K. A. Fletcher, and R. J. Leeper, Phys. Plasmas **17**, 056311 (2010).

29. D. G. Hicks, B. K. Spears, D. G. Braun, R. E. Olson, C. M. Sorce, P. M. Celliers, G. W. Collins, and O. L. Landen, Phys. Plasmas **17**, 102703 (2010).

30. J. P. Knauer, K. Anderson, R. Betti, T. J. B. Collins, V. Yu. Glebov, V. N. Goncharov, F. J. Marshall, D. D. Meyerhofer, P. B. Radha, S. P. Regan, C. Stoeckl, J. A. Frenje, C. K. Li, R. D. Petrasso, and F. H. Séguin, Bull. Am. Phys. Soc. **50**, 113 (2005).

31. C. Stoeckl, V. Yu. Glebov, S. Roberts, T. C. Sangster, R. A. Lerche, R. L. Griffith, and C. Sorce, Rev. Sci. Instrum. **74**, 1713 (2003).

32. T. J. Murphy *et al.*, Rev. Sci. Instrum. **66**, 930 (1995).

33. H. Brysk, Plasma Phys. **15**, 611 (1973).

34. J. M. Soures, R. J. Hutchison, S. D. Jacobs, L. D. Lund, R. L. McCrory, and M. C. Richardson, in *Proceedings of the 10th Symposium on Fusion Engineering* (IEEE, New York, 1983), p. 1392.

35. F. J. Marshall, S. A. Letzring, C. P. Verdon, S. Skupsky, R. L. Keck, J. P. Knauer, R. L. Kremens, D. K. Bradley, T. Kessler, J. Delettrez, H. Kim, J. M. Soures, and R. L. McCrory, Phys. Rev. A **40**, 2547 (1989).

36. R. L. McCrory, J. M. Soures, C. P. Verdon, F. J. Marshall, S. A. Letzring, S. Skupsky, T. J. Kessler, R. L. Kremens, J. P. Knauer, H. Kim, J. Delettrez, R. L. Keck, and D. K. Bradley, Nature **335**, 225 (1988).

37. D. L. Musinski *et al.*, J. Appl. Phys. **51**, 1394 (1980).

38. S. Kacenjar, L. M. Goldman, A. Entenberg, and S. Skupsky, J. Appl. Phys. **56**, 2027 (1984); S. Skupsky and S. Kacenjar, J. Appl. Phys. **52**, 2608 (1981).

39. J. Delettrez, R. Epstein, M. C. Richardson, P. A. Jaanimagi, and B. L. Henke, Phys. Rev. A **36**, 3926 (1987).

40. J. K. Hoffer and L. R. Foreman, Phys. Rev. Lett. **60**, 1310 (1988); A. J. Martin, R. J. Simms, and R. B. Jacobs, J. Vac. Sci. Technol. A **6**, 1885 (1988).

41. G. W. Collins *et al.*, J. Vac. Sci. Technol. A **14**, 2897 (1996).

42. *LLE Review Quarterly Report* **81**, 6, Laboratory for Laser Energetics, University of Rochester, Rochester, NY, LLE Document No. DOE/SF/19460-335 (1999).

43. T. R. Boehly, D. L. Brown, R. S. Craxton, R. L. Keck, J. P. Knauer, J. H. Kelly, T. J. Kessler, S. A. Kumpan, S. J. Loucks, S. A. Letzring, F. J. Marshall, R. L. McCrory, S. F. B. Morse, W. Seka, J. M. Soures, and C. P. Verdon, Opt. Commun. **133**, 495 (1997).

44. C. Stoeckl, C. Chiritescu, J. A. Delettrez, R. Epstein, V. Yu. Glebov, D. R. Harding, R. L. Keck, S. J. Loucks, L. D. Lund, R. L. McCrory, P. W. McKenty, F. J. Marshall, D. D. Meyerhofer, S. F. B. Morse, S. P. Regan, P. B. Radha, S. Roberts, T. C. Sangster, W. Seka, S. Skupsky, V. A. Smalyuk, C. Sorce, J. M. Soures, R. P. J. Town, J. A. Frenje, C. K. Li, R. D. Petrasso, F. H. Séguin, K. Fletcher, S. Padalino, C. Freeman, N. Izumi, R. Lerche, and T. W. Phillips, Phys. Plasmas **9**, 2195 (2002).

45. T. C. Sangster, R. Betti, R. S. Craxton, J. A. Delettrez, D. H. Edgell, L. M. Elasky, V. Yu. Glebov, V. N. Goncharov, D. R. Harding, D. Jacobs-Perkins, R. Janezic, R. L. Keck, J. P. Knauer, S. J. Loucks, L. D. Lund, F. J. Marshall, R. L. McCrory, P. W. McKenty, D. D. Meyerhofer, P. B. Radha, S. P. Regan, W. Seka, W. T. Shmayda, S. Skupsky, V. A. Smalyuk, J. M. Soures, C. Stoeckl, B. Yaakobi, J. A. Frenje, C. K. Li, R. D. Petrasso, F. H. Séguin, J. D. Moody, J. A. Atherton, B. D. MacGowan, J. D. Kilkenny, T. P. Bernat, and D. S. Montgomery, Phys. Plasmas **14**, 058101 (2007).

46. P. W. McKenty, T. C. Sangster, M. Alexander, R. Betti, R. S. Craxton, J. A. Delettrez, L. Elasky, R. Epstein, A. Frank, V. Yu. Glebov, V. N. Goncharov, D. R. Harding, S. Jin, J. P. Knauer, R. L. Keck, S. J. Loucks, L. D. Lund, R. L. McCrory, F. J. Marshall, D. D. Meyerhofer, S. P. Regan, P. B. Radha, S. Roberts, W. Seka, S. Skupsky, V. A. Smalyuk, J. M. Soures, K. A. Thorp, M. Wozniak, J. A. Frenje, C. K. Li, R. D. Petrasso, F. H. Séguin, K. A. Fletcher, S. Padalino, C. Freeman, N. Izumi, J. A. Koch, R. A. Lerche, M. J. Moran, T. W. Phillips, G. J. Schmid, and C. Sorce, Phys. Plasmas **11**, 2790 (2004).

47. F. J. Marshall, R. S. Craxton, J. A. Delettrez, D. H. Edgell, L. M. Elasky, R. Epstein, V. Yu. Glebov, V. N. Goncharov, D. R. Harding, R. Janezic, R. L. Keck, J. D. Kilkenny, J. P. Knauer, S. J. Loucks, L. D. Lund, R. L. McCrory, P. W. McKenty, D. D. Meyerhofer, P. B. Radha, S. P. Regan, T. C. Sangster, W. Seka, V. A. Smalyuk, J. M. Soures, C. Stoeckl, S. Skupsky, J. A. Frenje, C. K. Li, R. D. Petrasso, and F. H. Séguin, Phys. Plasmas **12**, 056302 (2005).

48. P. B. Radha, V. N. Goncharov, T. J. B. Collins, J. A. Delettrez, Y. Elbaz, V. Yu. Glebov, R. L. Keck, D. E. Keller, J. P. Knauer, J. A. Marozas, F. J. Marshall, P. W. McKenty, D. D. Meyerhofer, S. P. Regan, T. C. Sangster, D. Shvarts, S. Skupsky, Y. Srebro, R. P. J. Town, and C. Stoeckl, Phys. Plasmas **12**, 032702 (2005).

49. V. N. Goncharov, P. McKenty, S. Skupsky, R. Betti, R. L. McCrory, and C. Cherfils-Clérouin, Phys. Plasmas **7**, 5118 (2000).

50. T. R. Boehly, V. N. Goncharov, O. Gotchev, J. P. Knauer, D. D. Meyerhofer, D. Oron, S. P. Regan, Y. Srebro, W. Seka, D. Shvarts, S. Skupsky, and V. A. Smalyuk, Phys. Plasmas **8**, 2331 (2001).

51. K. Anderson and R. Betti, Phys. Plasmas **11**, 5 (2004).

52. S. Skupsky, R. W. Short, T. Kessler, R. S. Craxton, S. Letzring, and J. M. Soures, J. Appl. Phys. **66**, 3456 (1989).

53. W. L. Kruer, *The Physics of Laser–Plasma Interactions*, Frontiers in Physics, Vol. 73, edited by D. Pines (Addison-Wesley, Redwood City, CA, 1988).

54. R. C. Malone, R. L. McCrory, and R. L. Morse, Phys. Rev. Lett. **34**, 721 (1975).

55. L. Spitzer, Jr. and R. Härm, Phys. Rev. **89**, 977 (1953).

56. S. Chapman and T. G. Cowling, *The Mathematical Theory of Non-Uniform Gases; An Account of the Kinetic Theory of Viscosity, Thermal Conduction and Diffusion in Gases*, 3rd. ed. (Cambridge University Press, Cambridge, England, 1970).

57. V. N. Goncharov, T. C. Sangster, P. B. Radha, R. Betti, T. R. Boehly, T. J. B. Collins, R. S. Craxton, J. A. Delettrez, R. Epstein, V. Yu. Glebov, S. X. Hu, I. V. Igumenshchev, J. P. Knauer, S. J. Loucks, J. A. Marozas, F. J. Marshall, R. L. McCrory, P. W. McKenty, D. D. Meyerhofer, S. P. Regan, W. Seka, S. Skupsky, V. A. Smalyuk, J. M. Soures, C. Stoeckl, D. Shvarts, J. A. Frenje, R. D. Petrasso, C. K. Li, F. Séguin, W. Manheimer, and D. G. Colombant, Phys. Plasmas **15**, 056310 (2008).

58. N. A. Krall and A. W. Trivelpiece, *Principles of Plasma Physics* (San Francisco Press, Inc., San Francisco, 1986).

59. V. N. Goncharov and G. Li, Phys. Plasmas **11**, 5680 (2004).

60. V. A. Smalyuk, S. X. Hu, V. N. Goncharov, D. D. Meyerhofer, T. C. Sangster, D. Shvarts, C. Stoeckl, B. Yaakobi, J. A. Frenje, and R. D. Petrasso, Phys. Rev. Lett. **101**, 025002 (2008).

61. V. N. Goncharov, Phys. Rev. Lett. **82**, 2091 (1999).

62. O. Gotchev, V. N. Goncharov, J. P. Knauer, T. R. Boehly, T. J. B. Collins, R. Epstein, P. A. Jaanimagi, and D. D. Meyerhofer, Phys. Rev. Lett. **96**, 115005 (2006).

63. W. Seka, D. H. Edgell, J. P. Knauer, J. F. Myatt, A. V. Maximov, R. W. Short, T. C. Sangster, C. Stoeckl, R. E. Bahr, R. S. Craxton, J. A. Delettrez, V. N. Goncharov, I. V. Igumenshchev, and D. Shvarts, Phys. Plasmas **15**, 056312 (2008).

64. I. V. Igumenshchev, V. N. Goncharov, W. Seka, D. Edgell, and T. R. Boehly, Phys. Plasmas **14**, 092701 (2007).

65. A. Simon, R. W. Short, E. A. Williams, and T. Dewandre, Phys. Fluids **26**, 3107 (1983).

66. C. Stoeckl, V. Yu. Glebov, D. D. Meyerhofer, W. Seka, B. Yaakobi, R. P. J. Town, and J. D. Zuegel, Rev. Sci. Instrum. **72**, 1197 (2001).

67. V. A. Smalyuk, D. Shvarts, R. Betti, J. A. Delettrez, D. H. Edgell, V. Yu. Glebov, V. N. Goncharov, R. L. McCrory, D. D. Meyerhofer, P. B. Radha, S. P. Regan, T. C. Sangster, W. Seka, S. Skupsky, C. Stoeckl, B. Yaakobi, J. A. Frenje, C. K. Li, R. D. Petrasso, and F. H. Séguin, Phys. Rev. Lett. **100**, 185005 (2008).

68. H. N. Kornblum, R. L. Kauffman, and J. A. Smith, Rev. Sci. Instrum. **57**, 2179 (1986); K. M. Campbell *et al.*, Rev. Sci. Instrum. **75**, 3768 (2004).

69. T. C. Sangster, V. N. Goncharov, P. B. Radha, V. A. Smalyuk, R. Betti, R. S. Craxton, J. A. Delettrez, D. H. Edgell, V. Yu. Glebov, D. R. Harding, D. Jacobs-Perkins, J. P. Knauer, F. J. Marshall, R. L. McCrory, P. W. McKenty, D. D. Meyerhofer, S. P. Regan, W. Seka, R. W. Short, S. Skupsky, J. M. Soures, C. Stoeckl, B. Yaakobi, D. Shvarts, J. A. Frenje, C. K. Li, R. D. Petrasso, and F. H. Séguin, Phys. Rev. Lett. **100**, 185006 (2008).

70. T. R. Boehly, D. H. Munro, P. M. Celliers, R. E. Olson, D. G. Hicks, V. N. Goncharov, G. W. Collins, H. F. Robey, S. X. Hu, J. A. Marozas, T. C. Sangster, O. L. Landen, and D. D. Meyerhofer, Phys. Plasmas **16**, 056302 (2009).

71. L. M. Barker and R. E. Hollenbach, J. Appl. Phys. **43**, 4669 (1972); P. M. Celliers *et al.*, Appl. Phys. Lett. **73**, 1320 (1998).

72. V. N. Goncharov, T. C. Sangster, T. R. Boehly, S. X. Hu, I. V. Igumenshchev, F. J. Marshall, R. L. McCrory, D. D. Meyerhofer, P. B. Radha, W. Seka, S. Skupsky, C. Stoeckl, D. T. Casey, J. A. Frenje, and R. D. Petrasso, Phys. Rev. Lett. **104**, 165001 (2010).

73. T. R. Boehly, V. N. Goncharov, W. Seka, M. A. Barrios, P. M. Celliers, D. G. Hicks, G. W. Collins, S. X. Hu, J. A. Marozas, and D. D. Meyerhofer, Phys. Rev. Lett. **106**, 195005 (2011).

74. I. V. Igumenshchev, D. H. Edgell, V. N. Goncharov, J. A. Delettrez, A. V. Maximov, J. F. Myatt, W. Seka, A. Shvydky, S. Skupsky, and C. Stoeckl, Phys. Plasmas **17**, 122708 (2010).

75. C. J. Randall, J. R. Albritton, and J. J. Thomson, Phys. Fluids **24**, 1474 (1981).

76. S. X. Hu, V. N. Goncharov, P. B. Radha, J. A. Marozas, S. Skupsky, T. R. Boehly, T. C. Sangster, D. D. Meyerhofer, and R. L. McCrory, Phys. Plasmas **17**, 102706 (2010).